Numerical Simulation of Lee Wave Events over the Pyrenees

By Takehiko Satomura

Meteorological Research Institute, 1-1, Nagamine, Tsukuba, Ibaraki 305, Japan

and

Philippe Bougeault

Météo-France, Centre National de Recherches Météorologiques
42, av. G. Coriolis, 31057 Toulouse, France
(Manuscript received 31 August 1993, in revised form 12 January 1994)

Abstract

A two-dimensional, non hydrostatic, compressible model is used to simulate the airflow over the Pyrenees in two lee wave events (IOP-3 and IOP-9) during the PYREX program. For each case, the mean flow is initialized by a single upstream sounding. The bottom topography used in the model is taken from the real mountain profile after smoothing out the wavelength shorter than 10 km.

In all cases, the model simulates well several characteristics of the lee waves: the wavelength, amplitude, and position. This is a strong indication that the lee waves observed in these events were excited by non linear wave-wave interactions of long mountain waves, because the topographic forcing in the model has negligible spectral amplitude at the wavelength of the lee waves ($\sim$10 km). Sensitivity experiments show that the phases of the lee waves are very sensitive to a small change of the mean wind and that their amplitudes are increased by the addition of smaller-scale topography.

In both cases, the simulated downward momentum fluxes agree well with the observed fluxes around 4 km height: -15×10^4 N/m in IOP-3 and $+10 \times 10^4$ N/m in the third day of IOP-9. The simulated fluxes are, however, almost constant through the troposphere, while the observations show rapid decrease of absolute values above 4 km height. This overestimation of the simulated momentum fluxes in the upper half of the troposphere is caused by the overestimation of the amplitude of long mountain waves at these heights; these long mountain waves control the vertical profile of the momentum flux there. It is suggested that the time evolution of the mean wind and the lateral momentum flux divergence found in the real atmosphere give rise to this overestimation.

1. Introduction

Gravity waves induced by mountains have been attracting many researchers since they induce many severe and non-severe phenomena in the atmosphere: Foehn or downslope windstorms on the earth's surface, hanging clouds, roll clouds or clear-air turbulence around the mountain height level, etc. Deceleration of the mean wind is also one of the important effects of orographically induced gravity waves because the change of the mean wind results in an alteration of the mean (*i.e.*, large-scale) pressure distribution. It generally occurs at higher levels where the gravity waves dissipate for reasons such as critical level or overturning, and transfer their momentum to the mean wind.

In recent years, global circulation models have been found to over-estimate westerly wind in the northern hemisphere (see Palmer *et al.*, 1986, for example). Many researchers have tried to reduce this systematic westerly bias. Two methods to reduce it are now commonly used: envelope mountain and gravity-wave-drag parameterization. The method of envelope mountain augments mountain heights by considering blocking effects of subgrid scale valleys (*e.g.*, Wallace *et al.*, 1983). On the other hand, the gravity-wave-drag parameterization is intended to represent the effects of subgrid scale mountain waves. Thanks to these parameterizations, the westerly bias in general circulation models was reduced mainly in the stratosphere (Palmer *et al.*, 1986; McFarlane, 1987). So far, most of the gravity-wave-drag parameterization schemes were based on the hydrostatic two-dimensional mountain wave theory.

In the troposphere, another type of mountain wave is commonly observed: non-hydrostatic gravity waves trapped in lower atmosphere called lee

waves. It has been explored since the very beginning of mountain wave research (Scorer, 1949, for example) and continue to be an interesting subject for theoretical, observational and numerical studies (*e.g.*, Vergeiner, 1971; Smith, 1979; Sharman and Wurtele, 1983). Very recently, lee waves have drawn the new attention from the view point of the atmospheric momentum budget (Iwasaki *et al.*, 1989; Durran, 1991; Kim and Arakawa, 1991). Iwasaki *et al.* (1989) introduced a new type of gravity-wave-drag parameterization to improve the tropospheric westerly bias by including the effects of trapped gravity waves. Using simple two-dimensional numerical models, Kim and Arakawa (1991) and Durran (1991) showed the importance of nonhydrostatic trapped gravity waves on the momentum budget in the troposphere. Because lee waves are trapped waves, they are able to keep significant amplitudes even far downstream of the mountain. For the same reason, however, they seem to carry little momentum upward beyond the duct region. Therefore, the detailed processes whereby trapped gravity waves affect the mean flow are not yet clear, and studies looking into the substance of the momentum transport in the troposphere are still required.

Meanwhile, efforts to understand the mountain effects by observational study have also been made. The 1970 Colorado Lee Wave Program targeted the Rocky Mountains (*e.g.*, Lilly and Kennedy, 1973), the ALPEX program spread observational nets around and over the Alps (*e.g.*, Kuettner, 1986), and the PYREX program measured the dynamical influence of the Pyrenees mountains (Bougeault *et al.*, 1990, 1993). But, in general, observational data are gathered only at a single point or on a few aircraft tracks, and it is difficult to reconstruct the two- or three-dimensional structure of the mountain waves in detail by the observations alone.

On the other hand, numerical modeling offers a wealth of consistent information. Therefore, numerical studies of mountain waves initialized by the observed data are able to give supplementary information about these phenomena. This has been attempted in several studies since the pioneering work of Klemp and Lilly (1978) in the case of mountain waves over the eastern slope of the Colorado Rockies. Recently, Hoinka and Clark (1991) and Clark and Miller (1991) used a three-dimensional nested nonhydrostatic model in the case of ALPEX. They pointed out a strong horizontal variability of both the momentum flux and the pressure drag. While the momentum flux in the model was much larger than the observed one (Hoinka and Clark, 1991), Clark and Miller (1991) concluded that hydrostatic simulations are sufficient to describe the basic dynamics in their ALPEX case, except for strong dependence of the drag and momentum fluxes on resolution. The lee waves which the newest gravity-wave-drag parameterization uses as physical substance were, however, not studied in their papers.

In the case of England, Shutts (1992) and Shutts and Broad (1993) studied lee waves by using a three-dimensional nonhydrostatic model. The comparison of their simulated waves with observations revealed a high level of agreement, especially in the case of northern England (Shutts and Broad, 1993). However, they could not compare the simulated momentum flux to the one calculated from observation, because the momentum flux based on the observation was so sensitive to the averaging length that they could not obtain reliable values. In the case of a downslope windstorm in Western Australia, Blockley and Lyons (1994) simulated lee waves over the Darling Scarp by using a two-dimensional nonhydrostatic model. While they studied nonhydrostatic effects on the windstorm and effects of the mountain shape on pressure drag, they did not compared their results with observation in detail.

In the present study, we perform numerical simulations with a two-dimensional nonhydrostatic model to get two-dimensional information for two lee wave events observed in the PYREX program (Bougeault *et al.*, 1990, 1993) and we compare simulated results with observational data in detail. While only one lee wave event over the Pyrenees was observed during the ALPEX program (Hoinka, 1984), the PYREX program captured several such events (Bougeault *et al.*, 1993) in a dense observational network using various instruments. This program, accordingly, offers a good database for researchers investigating (nonhydrostatic) lee wave effects on the atmosphere.

2. Model Description

2.1 Governing equations

The numerical model used in this study is that developed by Satomura (1989) and Sasaki and Satomura (1991). The momentum, thermodynamic and continuity equations are written in Cartesian coordinates as:

$$\frac{\partial u_i}{\partial t} + u_j \frac{\partial u_i}{\partial x_j} + c_p(\Theta + \theta)\frac{\partial \pi}{\partial x_i} - \delta_{i3} g \frac{\theta}{\Theta} = -\frac{2}{3}\frac{\partial E}{\partial x_i} + \frac{\partial}{\partial x_j}\left\{ K_m \left(\frac{\partial u_i}{\partial x_j} + \frac{\partial u_j}{\partial x_i} \right) \right\}, \quad (2.1)$$

$$\frac{\partial \theta}{\partial t} + u_j \frac{\partial (\Theta + \theta)}{\partial x_j} = \frac{\partial}{\partial x_j}\left(\frac{K_m}{\sigma_\theta} \frac{\partial \theta}{\partial x_j} \right), \quad (2.2)$$

$$\frac{\partial \pi}{\partial t} + u_j \frac{\partial (\Pi + \pi)}{\partial x_j} + \frac{R_d(\Pi + \pi)}{c_v}\frac{\partial u_j}{\partial x_j} = \frac{R_d(\Pi + \pi)}{c_v(\Theta + \theta)}\frac{\partial}{\partial x_j}\left(\frac{K_m}{\sigma_\theta}\frac{\partial \theta}{\partial x_j} \right), \quad (2.3)$$

where

$$\Pi + \pi = \left(\frac{p}{p_0}\right)^{R_d/c_p}$$

and

$$\frac{d\Pi}{dz} = -\frac{g}{c_p\Theta}.$$

In the above, u_i ($i = 1, 2, 3$) are the three-dimensional wind vectors u, v, w, respectively, θ is the potential temperature deviation from a reference state Θ which is a function of z only, E is the subgrid scale turbulent kinetic energy, K_m is the eddy mixing coefficient for momentum and $\sigma_\theta = 1/1.5$, p is the pressure, $p_0 = 10^5$ Pa, R_d is the gas constant for dry air, c_p and c_v are the specific heat of dry air at constant pressure and at constant volume, respectively. Here the summation convention (*e.g.*, Aris, 1962) has been used with respect to the indices i and j.

The eddy mixing coefficient is determined by the E-ε closure model (Rodi, 1985) with a slight modification proposed by Detering and Etling (1985):

$$\frac{\partial E}{\partial t} + u_j\frac{\partial E}{\partial x_j} = \frac{\partial}{\partial x_j}\left(\frac{K_m}{\sigma_E}\frac{\partial E}{\partial x_j}\right) + P + G - \varepsilon, \quad (2.4)$$

$$\frac{\partial \varepsilon}{\partial t} + u_j\frac{\partial \varepsilon}{\partial x_j} = \frac{\partial}{\partial x_j}\left(\frac{K_m}{\sigma_\varepsilon}\frac{\partial \varepsilon}{\partial x_j}\right) - C_2\frac{\varepsilon^2}{E} + C_1\frac{\varepsilon}{E}(P+G)(1+C_3R_f), \quad (2.5)$$

where E and ε are the subgrid scale turbulent kinetic energy and its dissipation ratio, respectively,

$$P = 2K_mS_{ij}S_{ij} - \frac{2}{3}E\frac{\partial u_j}{\partial x_j}, \quad (2.6)$$

$$S_{ij} = \frac{1}{2}\left(\frac{\partial u_i}{\partial x_j} + \frac{\partial u_j}{\partial x_i}\right), \quad (2.7)$$

$$G = -g\frac{K_m}{\sigma_\theta}\frac{1}{\Theta}\frac{\partial(\Theta+\theta)}{\partial x_3}, \quad (2.8)$$

$$R_f = \begin{cases} \dfrac{-G}{P+G} & \text{for } {u_1}^2 + {u_2}^2 > {u_3}^2, \\ 0 & \text{for } {u_1}^2 + {u_2}^2 \le {u_3}^2, \end{cases} \quad (2.9)$$

$$K_m = C_\mu\frac{E^2}{\varepsilon}, \quad (2.10)$$

and

$$\sigma_E = 0.741, \quad \sigma_\varepsilon = 1.3, \quad C_\mu = 0.0256,$$
$$C_1 = 1.44, \quad C_2 = 1.9, \quad C_3 = 0.8. \quad (2.11)$$

In this study, a two-dimensional version of the model is used: every derivative with respect to the y-direction (*i.e.*, x_2) is set to zero in Eqs. (2.1)–(2.6). Whereas the model equations have been described in Cartesian coordinates, the equations are solved in transformed coordinates to apply them to irregular terrain surface. The transformed coordinates are non-orthogonal curvilinear coordinates generated by the computer as a pre-processing of the model. The generation method is an elliptic generation system proposed by Shieh (1984), where coordinate lines are orthogonal to the terrain surface. The maximum deviation of the coordinate line from the vertical is, however, only of the order of 10 m, because we use very gently-sloping terrain in this paper (see below).

We use a discretization method centered both in time and in space, with a grid system where all variables are located at the same points except the Exner functions π and Π, which are staggered in the vertical. A time-splitting method similar to Klemp and Wilhelmson (1978) is used for computational efficiency. An implicit method is also used to gain further efficiency in vertical derivatives of terms related to sound waves and to viscous terms. A fourth-order artificial viscous term is added to Eqs. (2.1), (2.2), (2.4) and (2.5) to damp small-scale computational modes.

Durran and Klemp (1982) showed that latent heat release strongly modifies the structure of mountain waves. Some stratiform clouds were observed on the windward side of the Pyrenees mountains during the observational periods we consider (Attié *et al.*, 1991), but the effect of condensation does not seem to be important in these cases (Richard, personal communication). For simplicity, we do not consider moisture effects at all in the present work.

2.2 Boundary conditions

At the lateral inflow boundary, the velocity normal to the boundary does not change in time (*i.e.*, $\partial u/\partial t = 0$). An Orlanski (1976) type extrapolation (Miller and Thorpe, 1981) is used at outflow boundary for u. Other variables are specified to be the same as the inner point both at inflow and outflow.

The upper boundary is a free-slip rigid wall with no heat flux. The lower boundary is rigid rough terrain with a roughness length $z_0 = 0.5$ m. The surface temperature is fixed at its initial value, which is the same as the initial air temperature at the same height. The lowest layer is assumed to be a constant flux layer and turbulent variables in the lowest layer are estimated by the method of Busch *et al.* (1976).

3. Description of the experiments

3.1 Numerical aspects

The integration domain is divided into 325 grids in the x-direction, with a centered area of constant 1 km resolution having 304 points. In order to keep lateral boundaries sufficiently far from the region of interest and also to save the computer resources, grid intervals on both sides of the 1 km grid region are stretched in the power of two. The outermost grid interval becomes 128 km and this grid system

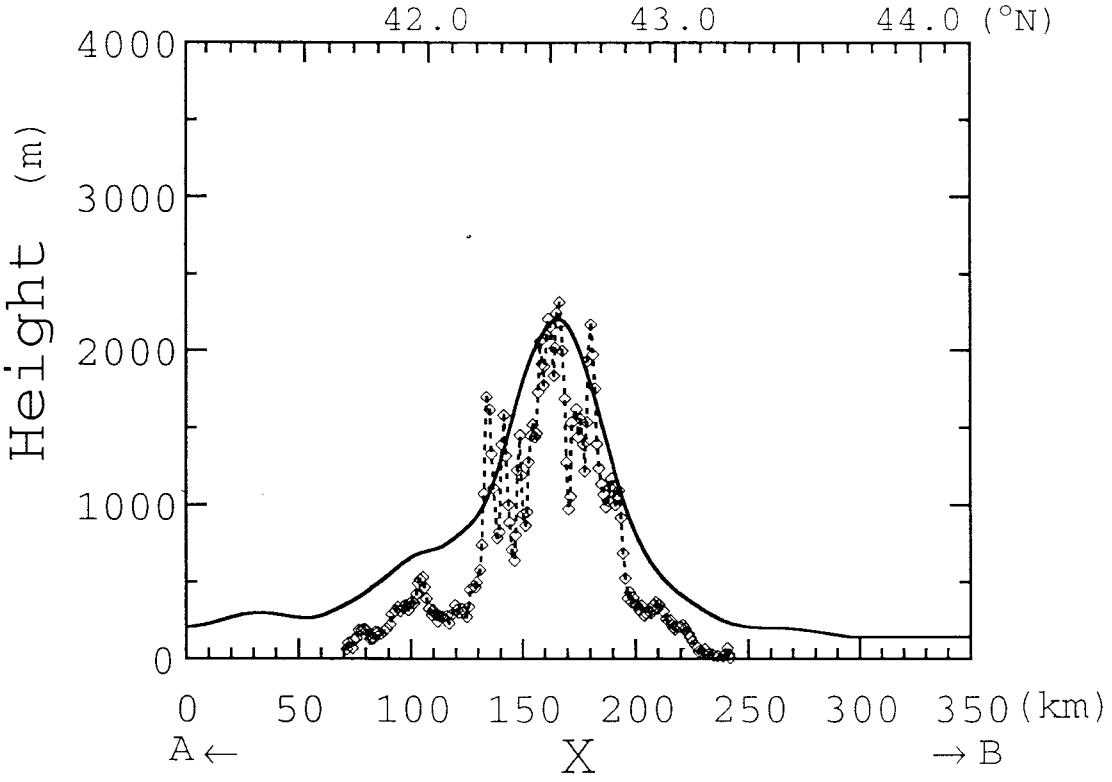

Fig. 1a. The profile of the model terrain. The dotted line with small rectangles is the topography observed by the airborne radar.

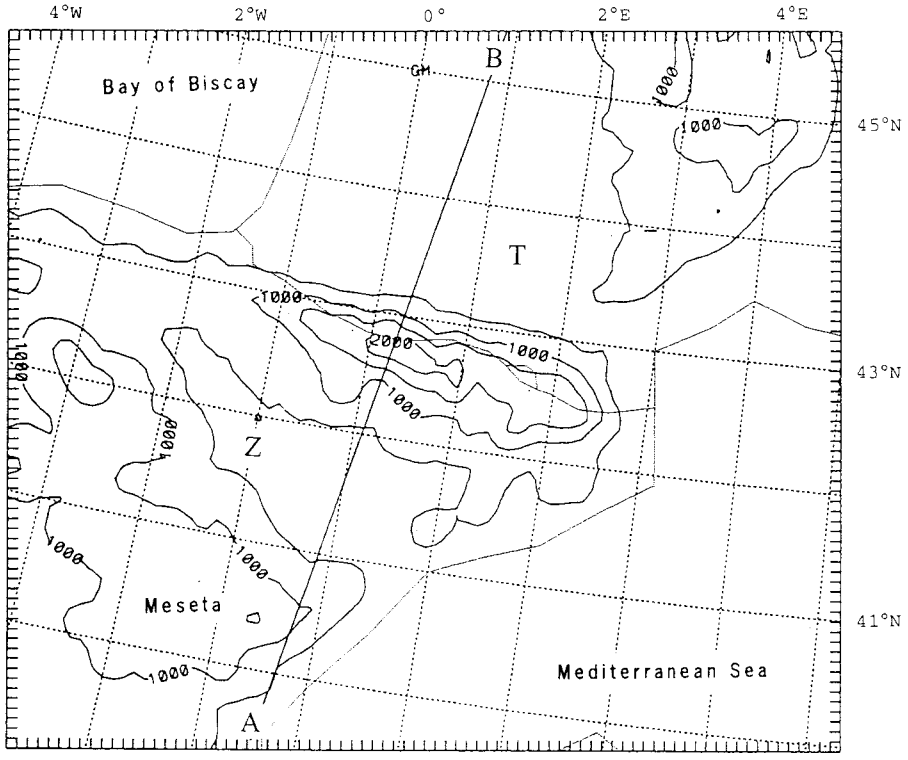

Fig. 1b. The topography around the Pyrenees mountains. The contour interval is 500 m, the line A-B is the section used in our 2-D model. Characters T and Z indicate two upper-air sounding stations, Toulouse and Zaragoza, respectively.

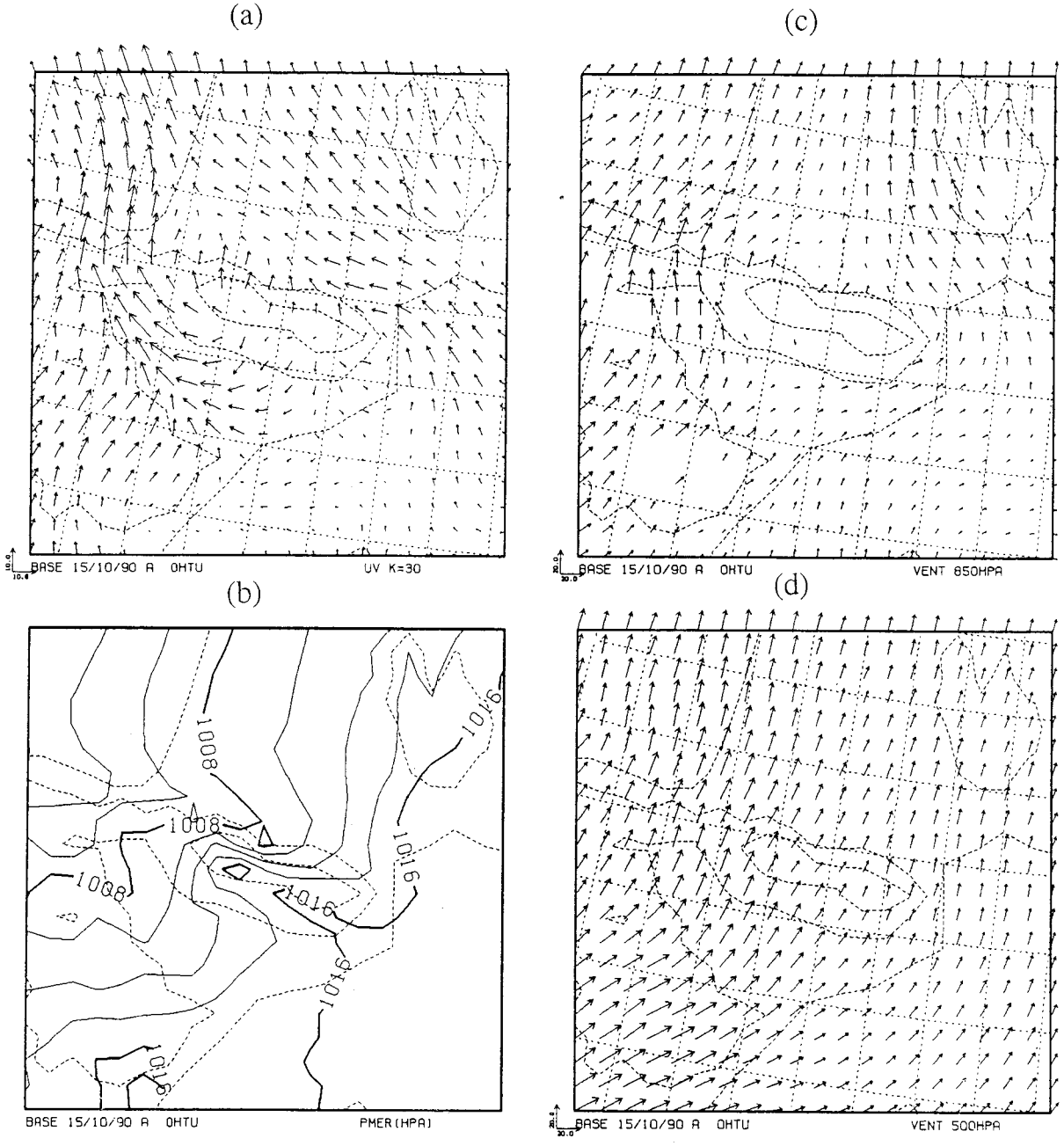

Fig. 2. Analysis of (a) surface wind, (b) sea surface pressure, (c) wind on 850 hPa isobaric surface and (d) wind on 500 hPa surface at 0600 UTC 15 October 1990 over south Europe. Dotted lines are contours of surface topography at 500 m intervals. The contour interval of sea surface pressure is 2 hPa. One grid length of wind arrow is 10 m/sec in (a), and is 20 m/sec in (c) and (d).

gives 815 km horizontal domain length in total. As a result of this stretching, the total mass of atmosphere in the model increases and, therefore, deceleration of horizontal velocity in time due to the surface friction is reduced. In nested models, such an abrupt change of grid interval as described above produces erroneous wave reflection (see for example, Phillips and Shukla, 1973; Kurihara *et al.*, 1979). To examine the effects of grid stretching in our model, we completed a simulation using a uniform grid interval (1 km) model with the same domain length as the stretched one. The comparison of the results in uniform grid model (not shown) with those in the stretched model reveals that these two models give almost the same results until 7 hours integration.

In the z-direction, the domain height is 22 km and is divided into 47 layers whose depths change with the height: from 30 m near the ground to 500 m in the free atmosphere. Above a height of 12 km, we put a sponge layer to avoid contamination by the re-

flection of vertically-propagating waves at the upper boundary. The short and long time steps in the time splitting procedure are 2 s and 10 s, respectively.

The model uses a smoothed terrain shape shown in Fig. 1a. This shape was originally taken from the topography in the central transect (Bougeault *et al.*, 1993) shown in Fig. 1b at 10 km resolution data. The terrain data were interpolated to a 1 km mesh by cubic spline functions, and the Meseta in Spain was wiped out, as shown in Fig. 1a, to avoid terrain height variation near the model boundary.

3.2 Synoptic situations and initial conditions of each experiment

There were 10 Intensive Observation Periods (IOPs, in the following) during the PYREX experiment. From these 10 IOPs, we chose two of four cases where significant lee waves were observed: IOP-3 and the third day of IOP-9. Lee waves were also observed on the first and the second days of IOP-9, but these cases are not suitable for our 2-dimensional simulation because the synoptic conditions in these cases indicate poor 2-dimensionality. In the following sub-sections, a brief description of the synoptic situations of these days and the model initial conditions are given (see Bougeault *et al.*, 1993, for brief descriptions of all IOPs).

3.2.1 IOP-3

This IOP started at 1800 (all time in UTC) on 14 October 1990 and ended at 1200 on 15 October 1990. As shown in Fig. 2, the synoptic wind around the Pyrenees was from southwest through the whole troposphere. In the layer below 850 hPa, however, the southwest wind was blocked and divided by the Pyrenees. A cyclone was developing over the eastern Atlantic Ocean. As a consequence, the vertical wind shear over the Pyrenees strengthened during the IOP-3 (not shown). This transient characteristic of the synoptic situation has been ignored in our simulation.

The potential temperature and wind soundings over Zaragoza at 0600 on 15 October 1990 are shown by solid lines in Fig. 3a and 3b, respectively. The temperature profile shows a strong inversion below 900 m height, and a nearly neutral layer of 1200 m depth above the inversion. The wind profile shows three strong shear layers (8000–9000 m, 3700–4600 m and below 700 m) and two moderate shear layers (4600–8000 m and 2000–3700 m).

The initial profiles used for experiment P3X1 (the reference experiment for the IOP-3) are shown by dashed lines in Fig. 3a and 3b. The initial temperature profile follows approximately the observation of Zaragoza below 10500 m and is extrapolated to the model top by using information from the Madrid sounding (upstream) at the same observation time. The tropopause is put at 12 km height and the stratosphere is assumed to be isothermal.

The initial wind profile is modified below 2000 m and above 8500 m height as shown in Fig. 3b. In the upper layer, the wind velocity follows airplane observations executed on the morning of 15 October. We have decided to slow down the wind velocity in the higher layers because the soundings were contaminated by the mountain wave at these altitudes (balloons did not rise vertically upstream of the Pyrenees, but flew over the Pyrenees). In contrast, the aircraft observations provide averaged wind values over 200 km length crossing the Pyrenees. They are more suitable for the model initial profile than raw-insonde soundings in the upper troposphere in this case. In the lower layers, we took account of the strong blocking effects by the mountain, which produce a weak wind region in the lower layers on the upstream side, as shown in Fig. 2a and 2c. Only three-dimensional models can manipulate this effect correctly.

The bottom topography in P3X1 is very smooth and the drag effect by the small-scale topography is not fully represented by only the surface roughness $z_0 = 0.5$ m. Therefore, in the experiment P3X2, the bottom topography is modified to study the effects of smaller-scale terrain on mountain waves under the same atmospheric conditions as in P3X1. The smaller-scale terrain is generated by a pseudo-random number generator in a computer library and the maximum of the random number is scaled to one quarter of the original mountain height. The random terrain is also restricted to have no amplitude at very short wavelengths (< 4 km) because terrain forcing of very short wavelengths excites computational modes in the model, and to have no amplitude in the region where the original mountain is lower than 300 m. The topography created as described above is shown in Fig. 4 and is used in P3X2. The initial wind and temperature are the same as P3X1.

In the experiment P3X3, the initial wind is decreased by 1 m/sec against P3X1, while the initial temperature profile and the bottom topography are the same as P3X1. Because the upstream sounding used to make the initial profile represents only a very local condition, it is possible that the initial profile is not suitable for simulating the observed event. This experiment P3X3 is designed to study the dependence of the simulated results on a small change of the initial velocity profile.

3.2.2 The third day of IOP-9

The anticyclone intensified over the eastern Atlantic during the night from 15 to 16 November. This resulted in nearly meridional winds at all levels. As shown in Fig. 5c and 5d, wind around the Pyrenees at 0600 on 16 November was northerly at 850 hPa and even a weak easterly component was present at 500 hPa. At the surface, strong blocking was noticed, as shown in Fig. 5a and 5b. This syn-

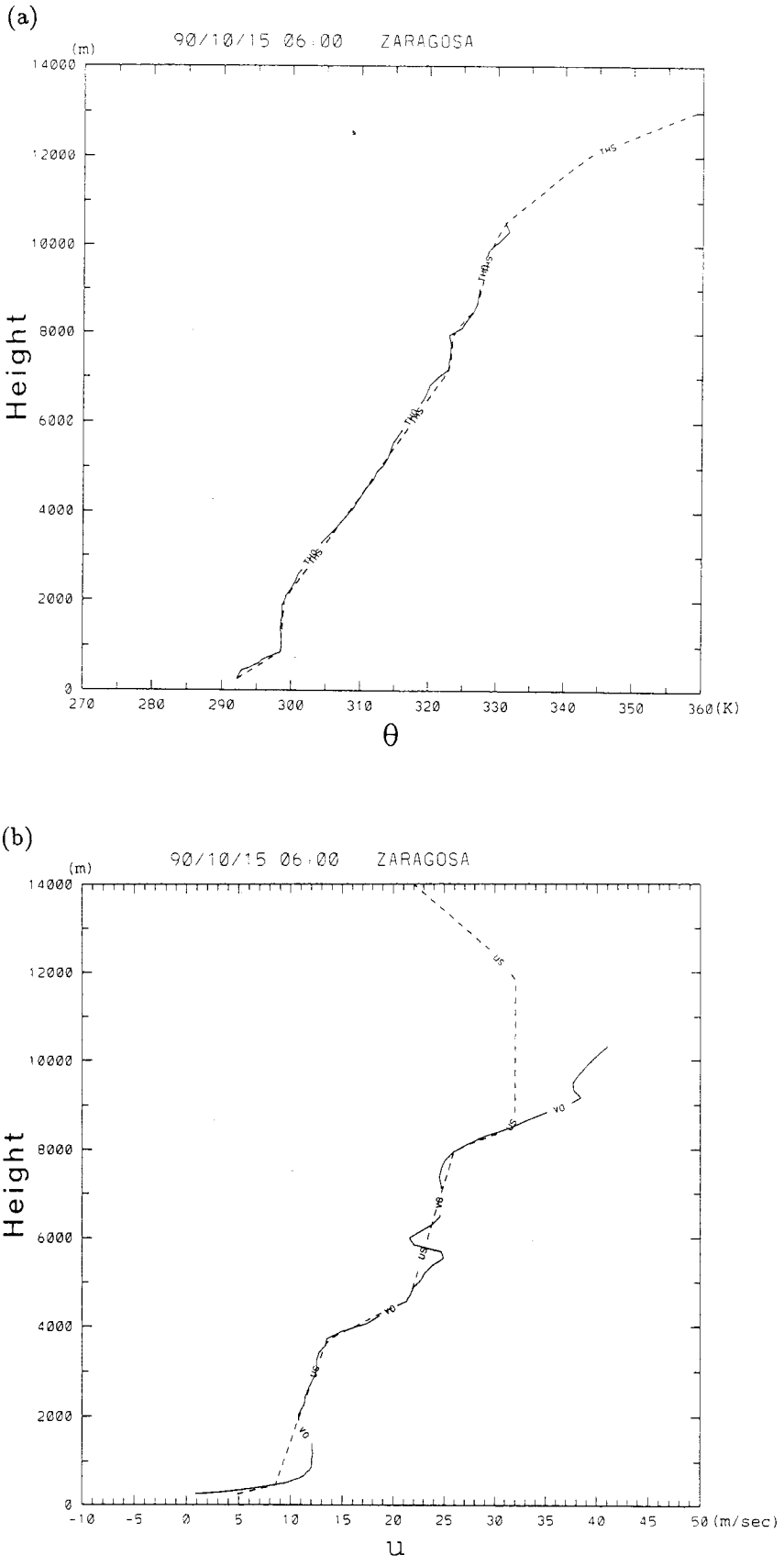

Fig. 3. Upper-air sounding over Zaragoza at 0600 UTC 15 October 1990 (solid line) and initial profile of the model (dashed line) for P3X1. (a) Potential temperature θ, (b) wind component parallel to the model plane (crossing the mountain). Wind velocity is positive when it blows from the south.

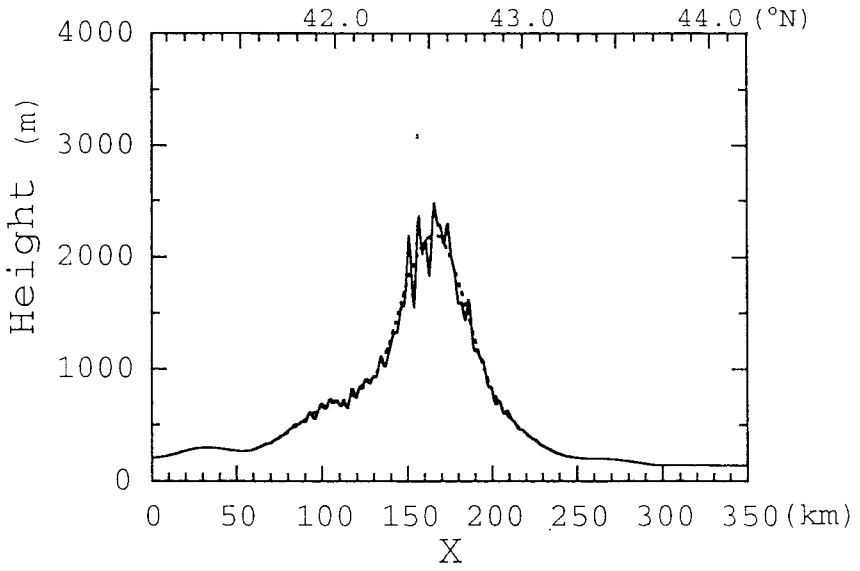

Fig. 4. The profile of the model terrain for P3X2. The dotted line is the topography used in P3X1.

optic pattern did not vary significantly through the day.

The potential temperature and wind soundings over Toulouse at 0600 on 16 November are shown in Fig. 6a and 6b, respectively. The temperature profile shows a stable layer below 4000 m height, including a thin (<~1000 m in depth) neutral layer around 1500 m height. The stability gradually decreased with height in the troposphere. The observed wind shows a rapid increase to 3500 m height followed by a constant velocity layer of 2000 m depth. Above 5500 m height, the wind increases linearly to the tropopause (~13 km).

Initial profiles for experiment P9D3 are shown by dashed lines in Fig. 6a and 6b. Both initial temperature and wind profiles approximately follow the observation of Toulouse 0600 UTC 16 November, except for the smoothing out of small fluctuations.[1]

4. Results

In this section, we present the results of numerical simulation after 6 hours integration, and compare them with observations. This integration time is chosen because the simulated mountain waves become quasi-steady.

4.1 IOP-3

4.1.1 P3X1

The potential temperature field after 6 hours of integration is shown in Fig. 7 (only a central part of the full domain is shown). This figure clearly shows three lee waves in the middle troposphere, followed by two smaller undulations in the lower atmosphere. The large lee waves have wavelengths of 12–13 km and amplitudes of ~0.5 km. The trailing lee waves have smaller amplitudes (<~0.5 km) and shorter wavelengths (~7 km). These waves are superimposed on a large amplitude (~2.5 km in peak-to-peak) long wavelength (>~80 km) mountain wave (called hereafter the principal wave).

While the reason why the large amplitude lee waves are restricted to extend to only three wavelengths is not clear, the generation mechanism of lee waves in this case is certainly as follows: these lee waves are produced by the non-linearity of the principal wave such as an oscillatory bore generation process (Christie, 1989), because we use a very smooth mountain shape which directly excites negligible amplitude around 12 km wavelength. This suggestion was confirmed by an additional experiment with reduced mountain height (10 m maximum) and the same atmospheric initial conditions. In this additional experiment, no such lee wave appeared in a simulation (not shown).

Some potential temperature undulations caused by lee waves reach the surface after the 210 km point. Undulations by lee waves near the surface are also seen both in the turbulence kinetic energy E (Fig. 8) and the horizontal wind (Fig. 9). If the synoptic wind is not exactly steady, which is a natural situation in the real atmosphere, the lee waves would neither be steady nor stationary. Such movement of lee waves would cause a drift of the high turbulence region near the surface, and, therefore it is probably responsible for the oscillations of friction velocity observed by the sodar at Lannemezan, as pointed by Bougeault *et al.* (1993).

The turbulence kinetic energy (Fig. 8) has a max-

[1]The neutral layer around 1500 m height (just below the mountain height) is a local feature because it is not observed by the sounding over Pau (about 150 km west by south from Toulouse). The results with this neutral layer in the initial profile (not shown) differ only a little from the results without this layer (*i.e.*, P9D3).

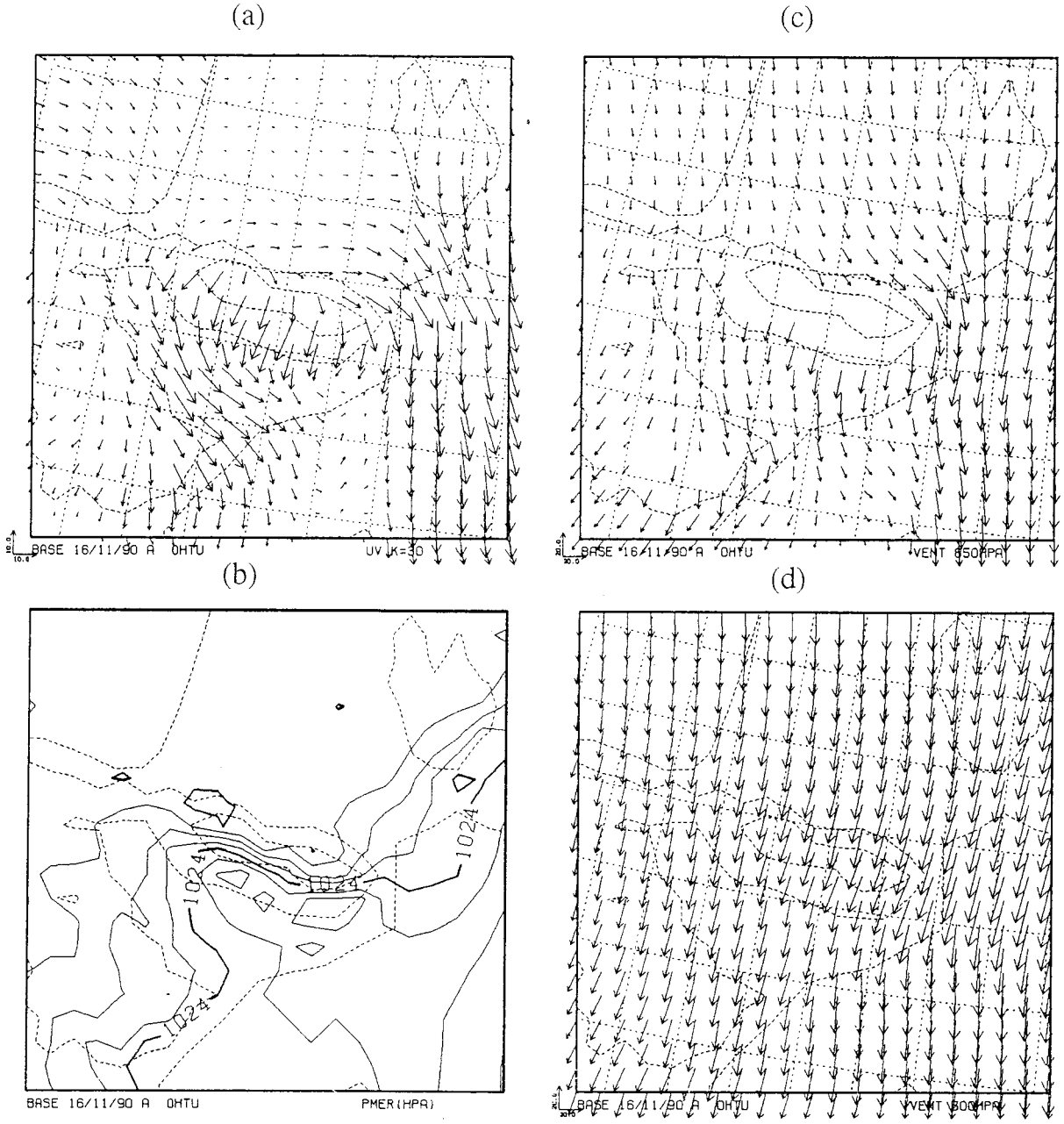

Fig. 5. Same as Fig. 2, except at 0600 UTC 16 November 1990.

imum of $10\,m^2/sec^2$ at some hundreds of meters above the ground on the lee side of the mountain. This value and its position are comparable to the observed maximum of $5.7\,m^2/sec^2$ about 500 m height near the 190 km point (not shown). It should also be noted that in the middle and the upper troposphere the turbulence kinetic energy is less than 0.1 m^2/sec^2. This fact indicates that overturning of the principal wave does not occur in the model. This agrees with the reports of on-board scientists of research airplanes (Attié *et al.*, 1991), and contrasts with the severe downslope windstorm event in central Colorado on 11 January 1972 where strong turbulence was reported through the troposphere (Lilly, 1978).

Although the horizontal wind is decelerated in the upper troposphere as gravity-wave-drag parameterizations in large-scale models expect, the horizontal velocity varies significantly both in the vertical and in the horizontal direction as shown in Fig. 9. A maximum wind of more than 32 m/sec occurs just behind the mountain peak around 3 to 4 km height, extending down close to the surface. On the lee side, the horizontal wind exhibits undulations producing multiple strong wind areas on the lee slope. In the middle troposphere, a rather complicated structure due to the superposition of lee waves on the principal wave is simulated, while the upstream side is

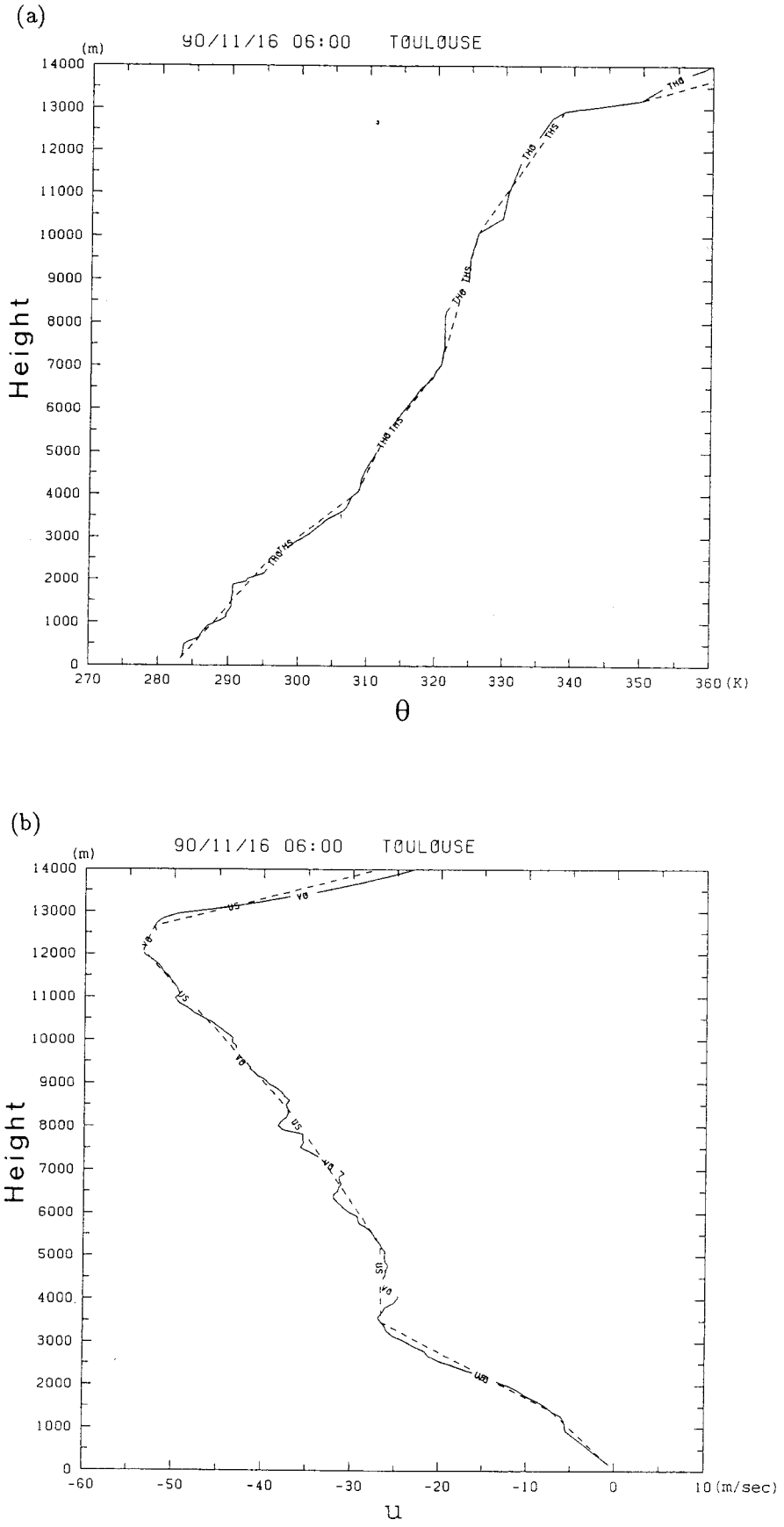

Fig. 6. Same as Fig. 3, except for upper-air sounding over Toulouse at 0600 UTC 16 November 1990 (solid line) and initial profile of the model (dashed line) for P9D3.

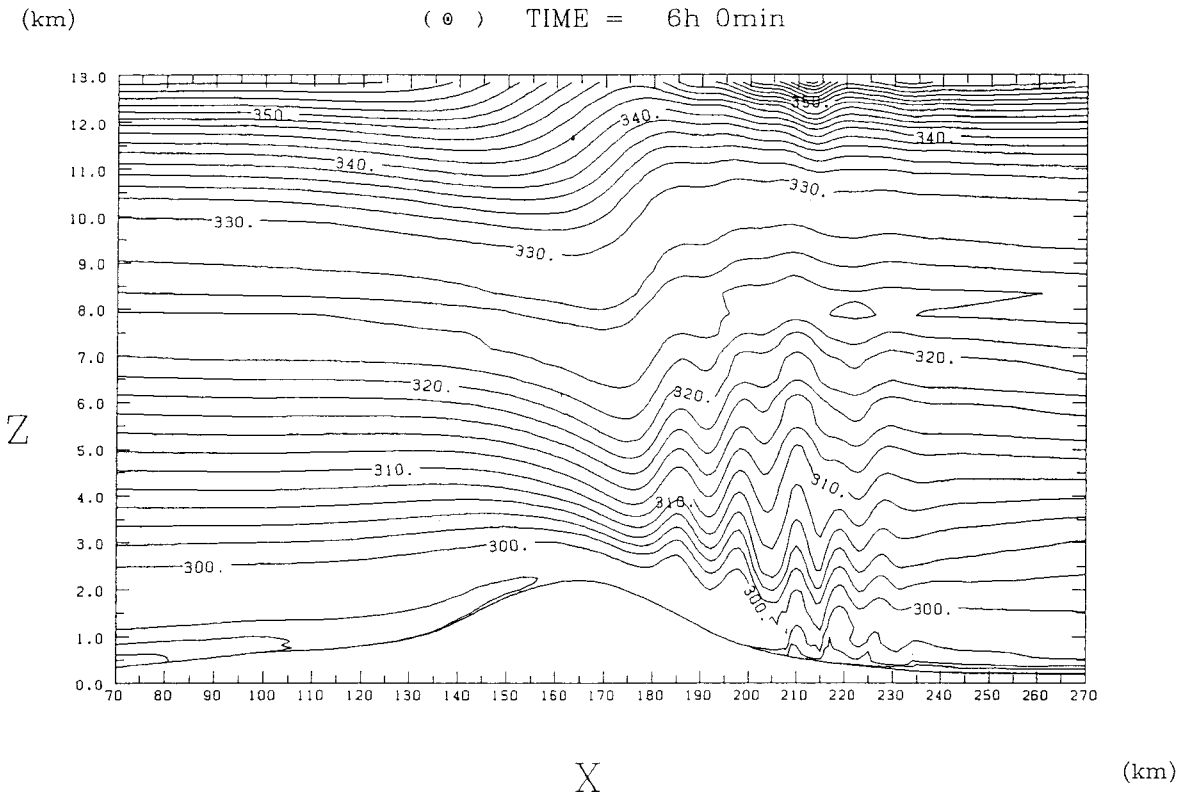

Fig. 7. Potential temperature around the mountain after 6 hours of integration in P3X1. The abscissa is the x-direction in km and the ordinate is the height in km. The contour interval is 2 K.

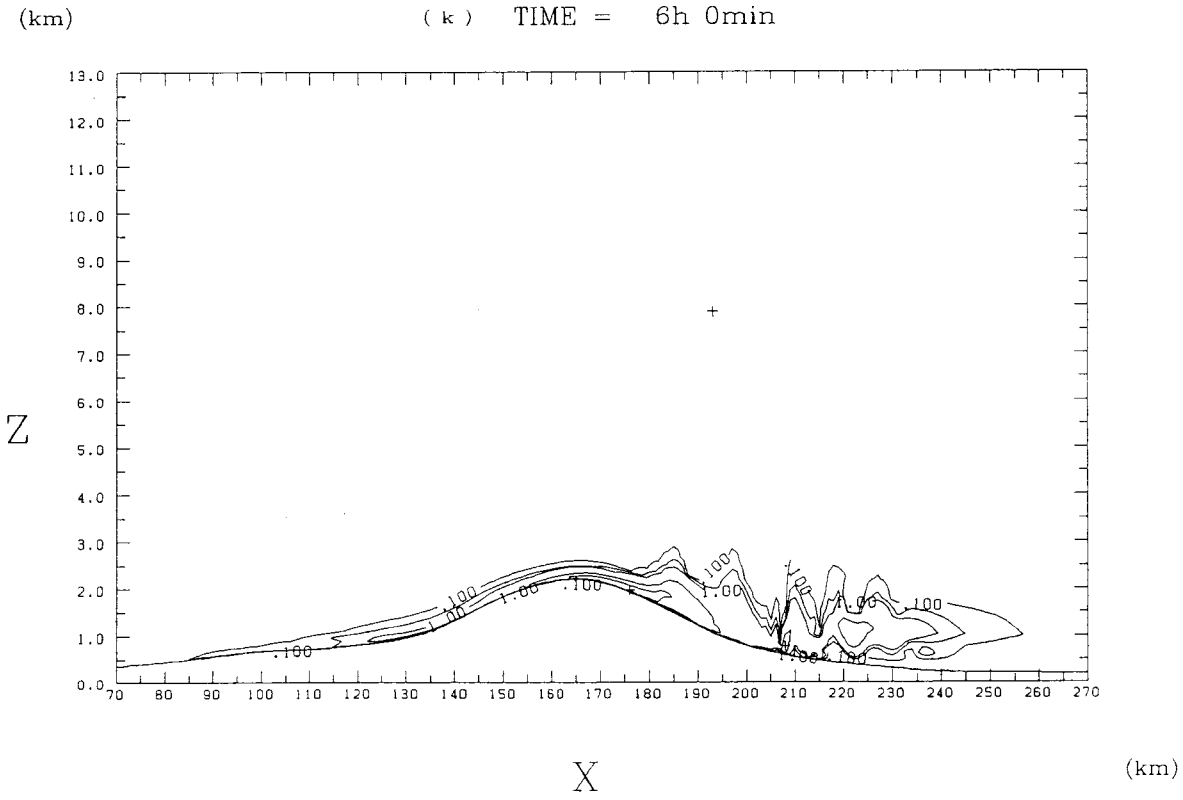

Fig. 8. Same as Fig. 7, except for subgrid scale turbulent kinetic energy calculated by E-ε model. The contour interval is logarithmic (0.1, 0.5, 1, 5, 10) in m^2/sec^2.

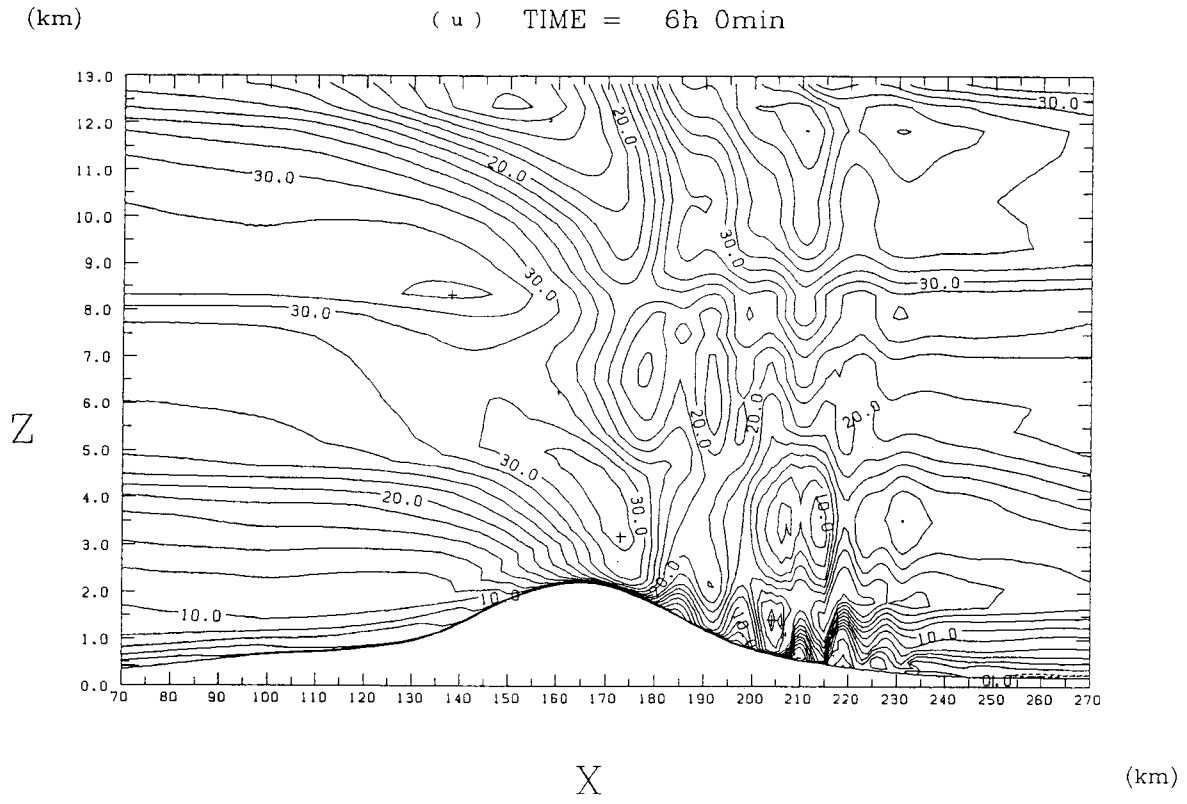

Fig. 9. Same as Fig. 7, except for horizontal wind. The contour interval is 2 m/sec.

accelerated and the lee side is decelerated in general.

Combining Figs. 8 and 9, we see that the main stream separates from the surface behind the point at 210–220 km, and some weak positive or negative velocity appears below a few hundreds meters above the ground. This weak wind corresponds well with the sheltered area observed by the surface meso-network (Bougeault *et al.*, 1993).

Horizontal variations of $u' = u - \bar{u}$ and $w' = w - \bar{w}$ on four isobaric surfaces are shown in Fig. 10a and b, respectively, where the overbar represents the horizontal average. This figure clearly shows that the model simulates the lee wave's amplitude and wavelength quite well, while their position in the model is about one wavelength (~10 km) behind the observation. This difference in the phase is not considered a serious problem, because a small change of the mean horizontal velocity improved this phase difference as shown in the later sub-section (experiment P3X3). On the other hand, the amplitude of the principal wave in horizontal velocity (Fig. 10a) is too large at 345 hPa and 217 hPa.

We have computed from the model outputs the vertical flux of horizontal momentum,

$$M_x = \int_{L_1}^{L_2} \rho u' w' dx, \tag{4.1}$$

and that by long mountain wave,

$$\hat{M}_x = \int_{L_1}^{L_2} \rho \hat{u}' \hat{w}' dx, \tag{4.2}$$

where $\hat{u}'$ and $\hat{w}'$ are the horizontal and the vertical perturbation velocity that have wavelengths longer than 17 km, and the line integration is completed from $L_1 = 75$ km to $L_2 = 245$ km. These fluxes are shown in Fig. 11 (see Appendix for the model performance in case of the linear mountain wave). Figure 11 obviously shows that long mountain waves control the vertical momentum flux. This agrees with a theoretical consideration that trapped waves do not transport momentum flux vertically.

In Fig. 11, the value of M_x observed by the airplanes is also shown (reproduced from Table 4 in Bougeault *et al.*, 1993). The observed momentum flux rapidly increases from -1.5×10^5 N/m to -0.15×10^5 N/m above 4 km height. This rapid increase (or reduction of the absolute value) of observed momentum flux in the vertical direction is an expected profile when lee waves are fully developed (Durran, 1991; Kim and Arakawa, 1991). The momentum flux in the model, however, keeps a nearly constant value of -1.5×10^5 N/m up to 10 km. This is about a 3 times overestimation, except at 4 km height.

We consider that the rather straight profile of M_x in the model is a natural result in our 2-dimensional model, because the linear theory states that the mo-

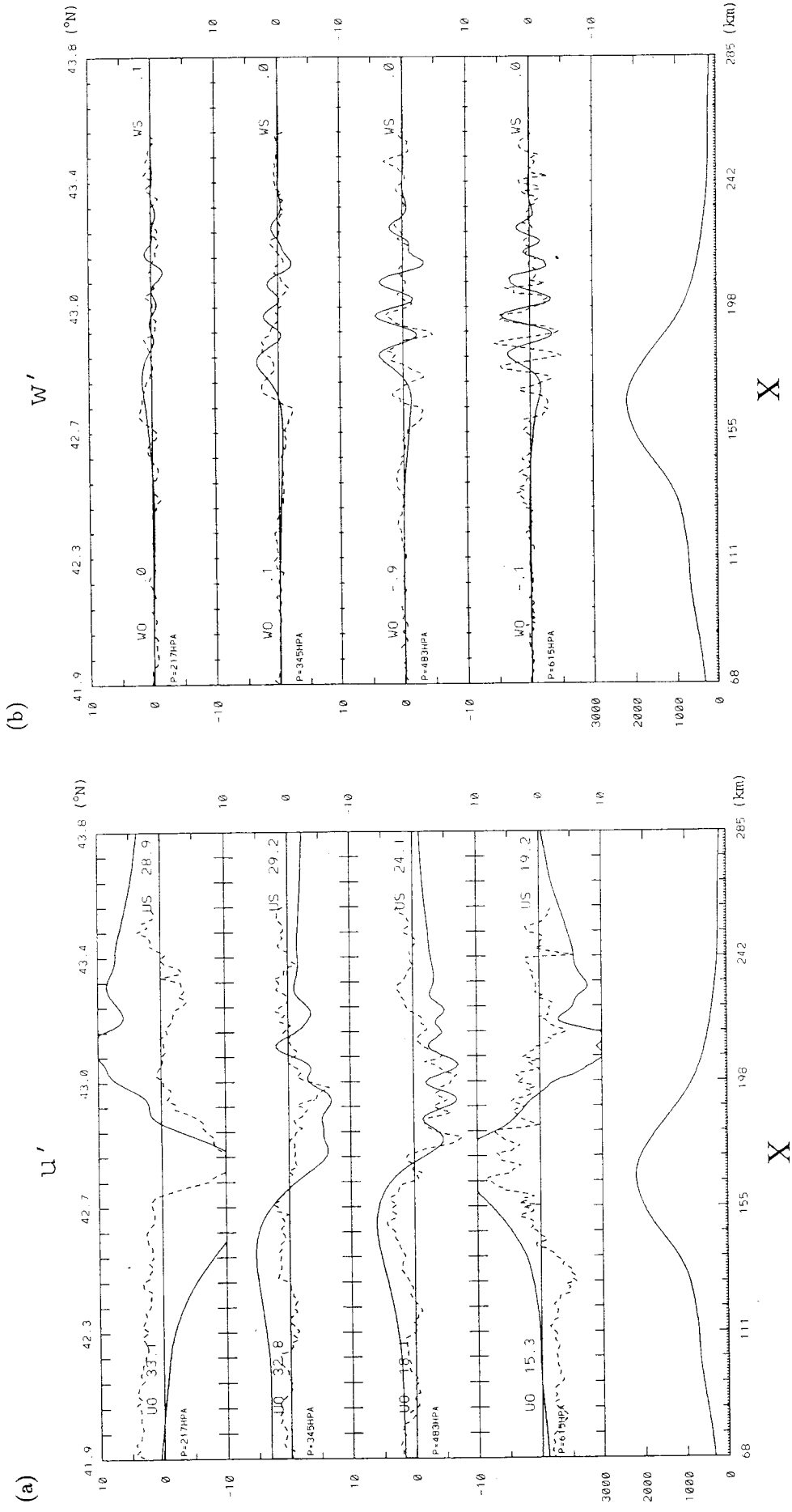

Fig. 10. Horizontal variation of (a) u' (m/sec) and (b) w' (m/sec) on isobaric surfaces (the top 4 figures) and model topography (the bottom figure). The solid and the dashed lines in the top 4 figures are the model results of P3X1 and the observed variation along the central transect by research airplanes on the morning of 15 October 1990, respectively. The isobaric surfaces are 217 hPa, 345 hPa, 483 hPa and 615 hPa from the top to the bottom, respectively. The mean values are noted on the left for the observation and on the right for the model results in each figure.

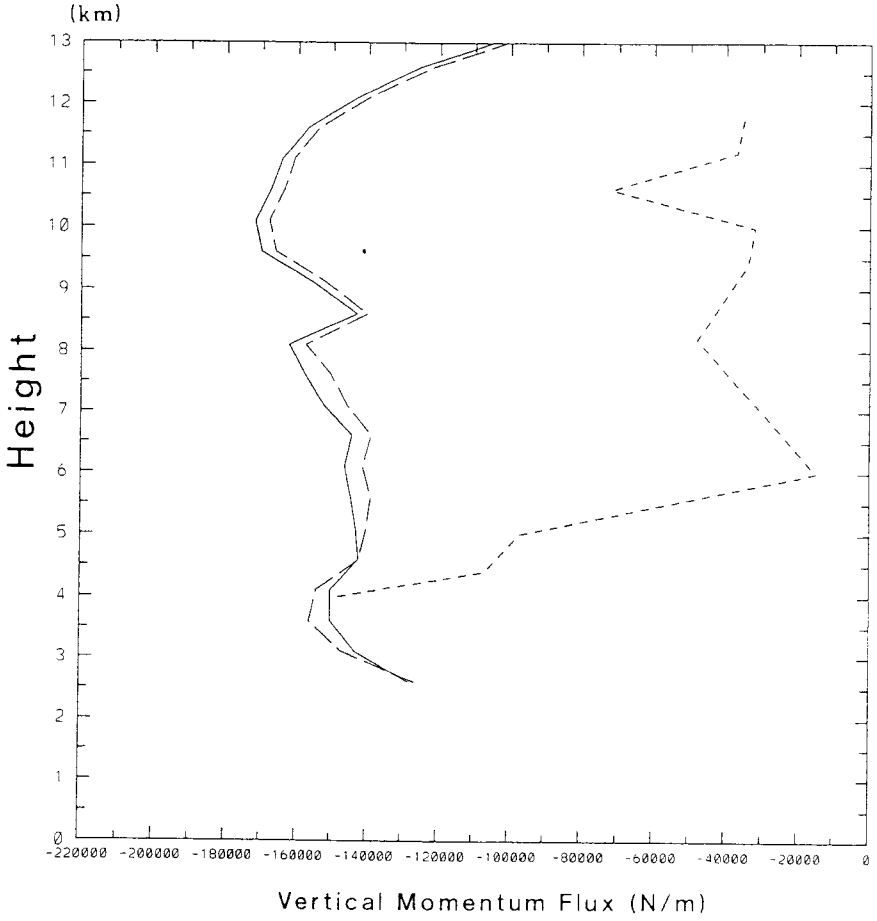

Fig. 11. Vertical profile of momentum flux M_x in the model (solid line) and observed by airplanes (short dashed line). The long dashed line is the vertical momentum flux by long mountain waves.

mentum flux must be constant if the mean velocity $U \neq 0$ in the inviscid atmosphere (*ex.*, Eliassen and Palm, 1961). The wave characteristics in this case would be described approximately by the linear theory and M_x should be approximately constant because the principal wave does not produce strong turbulence due to the wave overturning which causes the strong viscosity and, consequently, the deviation from the linear inviscid theory. The overestimation of M_x is also consistent with the overestimation of the amplitude of the principal wave. The reason why the observed principal wave has much smaller amplitude than the simulated one will be discussed later.

The pressure drag in the model is about 2 Pa × 175 km. This value is about twice the momentum flux M_x at 4 km height. This fact that only a small fraction of the surface pressure drag propagates to the free atmosphere agrees with the results of Hoinka and Clark (1991). The excess of pressure drag should be dissipated in the layer between the surface and the 4 km height, especially in the boundary layer. On the other hand, the observed pressure drag is about 6 Pa (Bougeault *et al.*, 1993), three times larger than the simulated value. We attribute this difference to the fact that observed pressure drag includes the geostrophic component of the pressure difference. The magnitude of this geostrophic component of the pressure difference is, however, very difficult to identify in the observation across the mountain. Therefore a straightforward comparison between the observed pressure drag and the one calculated by a 2-dimensional model which includes no Coriolis effect is meaningless.

4.1.2 P3X2

The horizontal variation of w' of P3X2 is shown in Fig. 12. In contrast to P3X1, the bottom topography in P3X2 directly excites mountain waves of wavelength around 12 km with certain amplitude. Lee waves in P3X2 are, therefore, stronger than those in P3X1, and more than four significant waves appear. The phase difference between the simulated and observed lee waves is practically the same as in P3X1, and the profile of the momentum flux M_x (not shown) is also almost the same as P3X1.

There is another way to incorporate the drag effects of the small topography: increasing the surface roughness. We examined its effect by increasing z_0

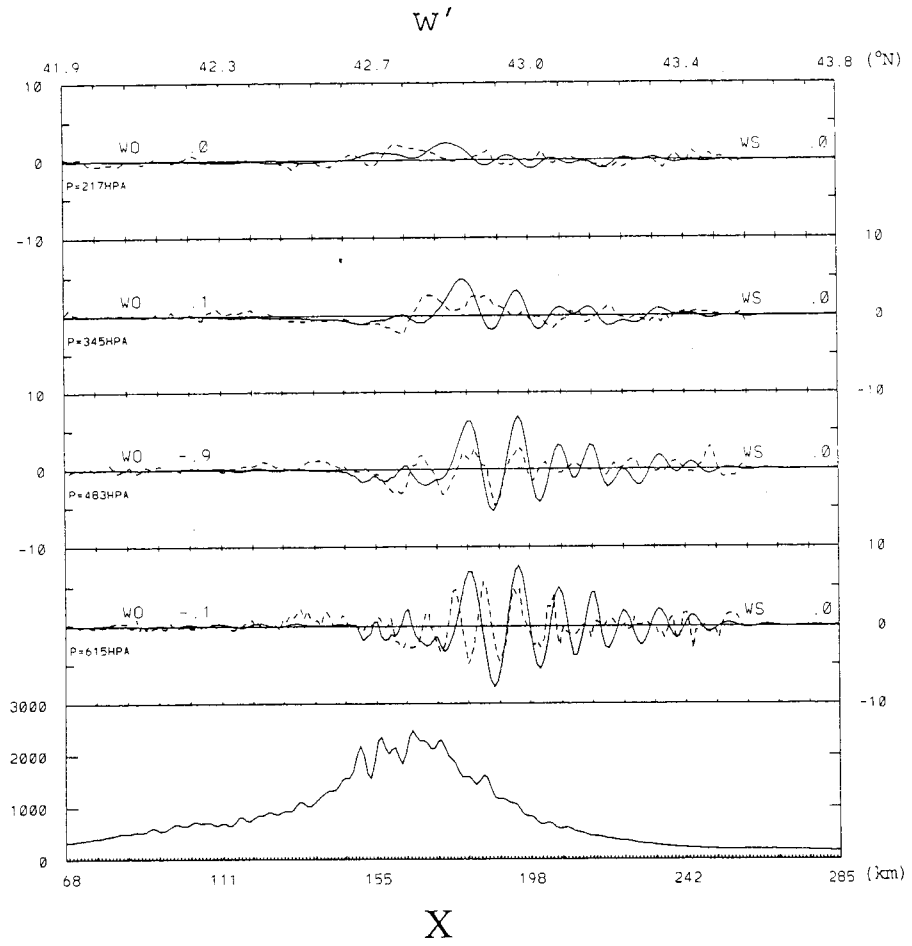

Fig. 12. Same as Fig. 10b, except for P3X2.

to 10 m, but the results were again almost the same as in P3X1. Therefore, neither the smaller-scale topography in this case nor a larger surface roughness can change the basic characteristics of mountain waves, though the former creates small-scale features in the horizontal variations of the waves and excites stronger lee waves. The small sensitivity of lee waves to z_0 is also found in Shutts and Broad (1993).

4.1.3 P3X3

Horizontal variation of w' of P3X3 is shown in Fig. 13. Comparing Fig. 10b, it is found that only 1 m/sec modification of the mean velocity improves the phase of the simulated lee waves by up to $\pi/2$, though the amplitudes of the lee waves are about half of P3X1. On the other hand, the amplitude of the principal wave is reduced only a little and the wavelength of the lee waves is unchanged.

Looking into Fig. 10a, it is noticed that the simulated mean horizontal velocity in the lower (higher) layer in P3X1 is 3–5 m/sec slower (faster) than the observed velocity. Therefore, we consider that the discrepancy of the phase of the lee wave between the simulation in P3X1 and the observation is explained by the difference of the mean velocity between the real atmosphere and the simulation.

If we want to make the simulated results more close to the observation, we have to tune the initial horizontal velocity by trial and error. We do not adjust, however, the initial profile further because we think it would not be worth doing in our two-dimensional model which can represent neither three-dimensional effects such as the flow deviation in the lower layer nor the time evolution of the synoptic situation.

The vertical momentum flux M_x (not shown) differs very little from that of P3X1 except the absolute value of the mean value decreased to $1.3\sim1.4 \times 10^5$ N/m. Considering the decreased lee-wave amplitude in P3X3, this indicates again that the principal wave transports the major part of the vertical momentum flux.

4.2 P9D3

The potential temperature field after 6 hours of integration in the case of P9D3 is shown in Fig. 14. This figure shows a well-established train of lee waves below 6 km height. These lee waves have wavelength of ~13 km and a maximum amplitude

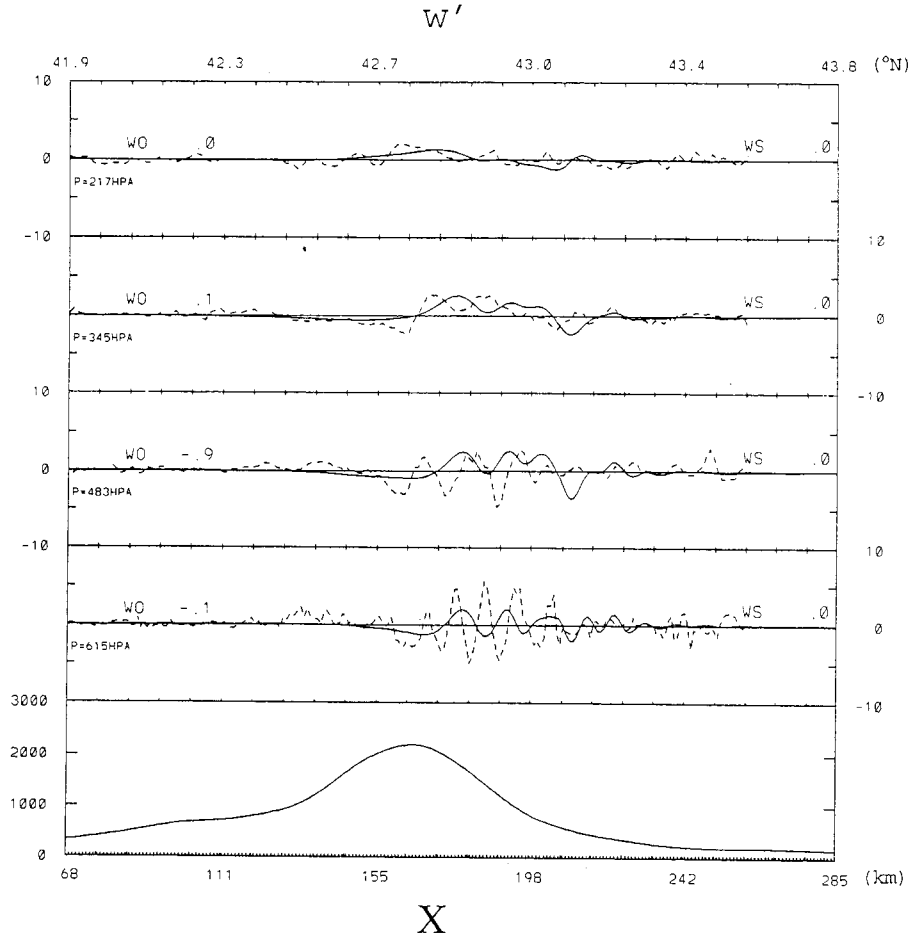

Fig. 13. Same as Fig. 10b, except for P3X3.

of ~0.7 km. Above that height, almost no wave activity is found owing to the less stable layer (*i.e.* small Scorer parameter; see next section) from 7 to 10 km height. The wave crest just downstream of the mountain peek is very steep and an overturning or strong turbulence is expected.

Indeed, the simulated turbulence kinetic energy shown in Fig. 15 presents a large and strong turbulence area which extends up to a height of 5 km and spreads downstream about 70 km in length. It has a maximum of 10 m^2/sec^2 around 2 km height over 130–140 km points. The area of turbulence corresponds well with the on-board scientists' reports (Attié *et al.*, 1991) marked by crosses in Fig. 15. The spread of the area of strong turbulence to downstream is probably caused by advection of the strong turbulence energy which originates in the wave-overturning area over 130–140 km points.

The maximum value and its position of simulated turbulence kinetic energy are also comparable to the observed maxima of 7.2 m^2/sec^2 at ~2000 m height over ~135 km point and 6.8 m^2/sec^2 at ~2500 m height over ~135 km point (not shown). It should also be noted that in the middle and the upper troposphere the turbulence kinetic energy is less than 0.1 m^2/sec^2 in the simulation and this agrees with the observation.

As seen by the horizontal variations of u and w shown in Fig. 16a and b, respectively, the model simulates the wavelength of the lee waves well. Both the amplitudes of lee waves and of the principal wave are, however, overestimated compared with the airplane observation.

The amplitude overestimation of the principal wave produces the overestimation of the vertical momentum flux as seen in Fig. 17. In this figure, we find that the momentum flux deduced from the observation decreased from 10×10^4 N/m at 3.5 km to zero around 5.5 km, then it increased to $\sim 2 \times 10^4$ N/m, while the simulated values decreased from 9.5×10^4 N/m at 4 km to 6×10^4 N/m at 6 km and then became constant. It is noteworthy that lee waves contribute negligibly to the momentum flux because the profiles of momentum fluxes M_x and $\hat{M}_x$ are almost the same above 4 km height. Below the 4 km height, however, these two profiles separate out, probably owing to the strong dissipation of lee waves by the turbulence in these heights.

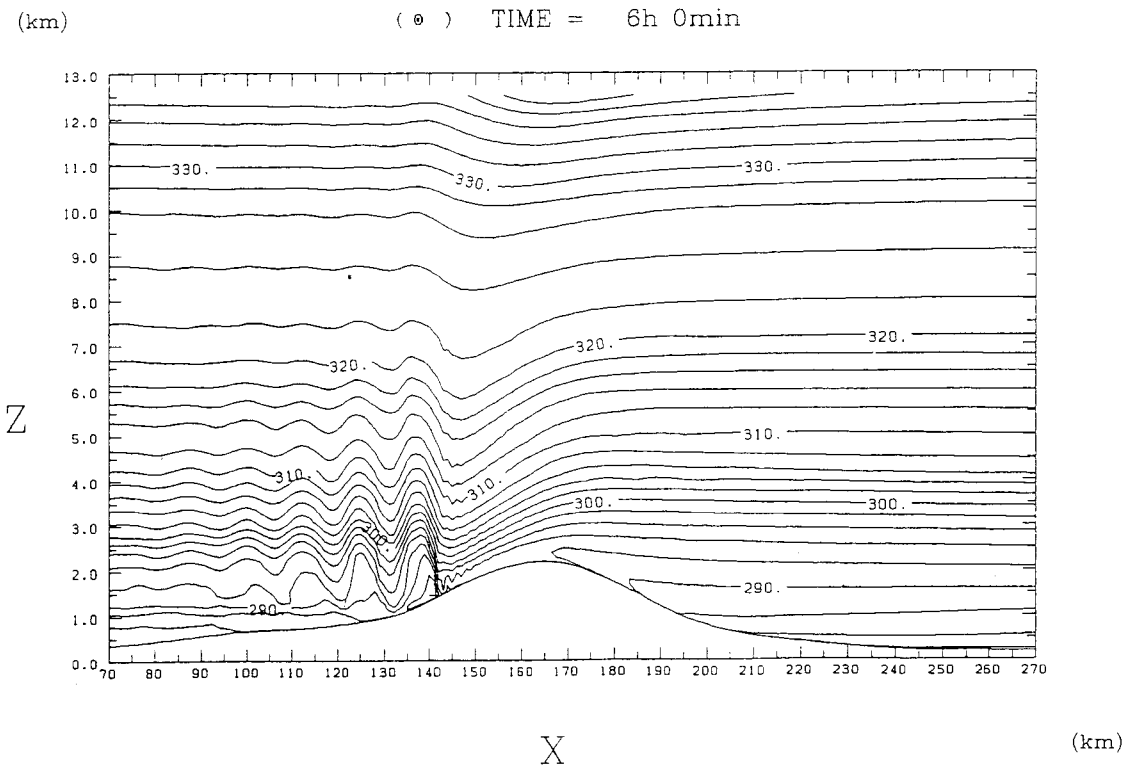

Fig. 14. Same as Fig. 7, except for P9D3.

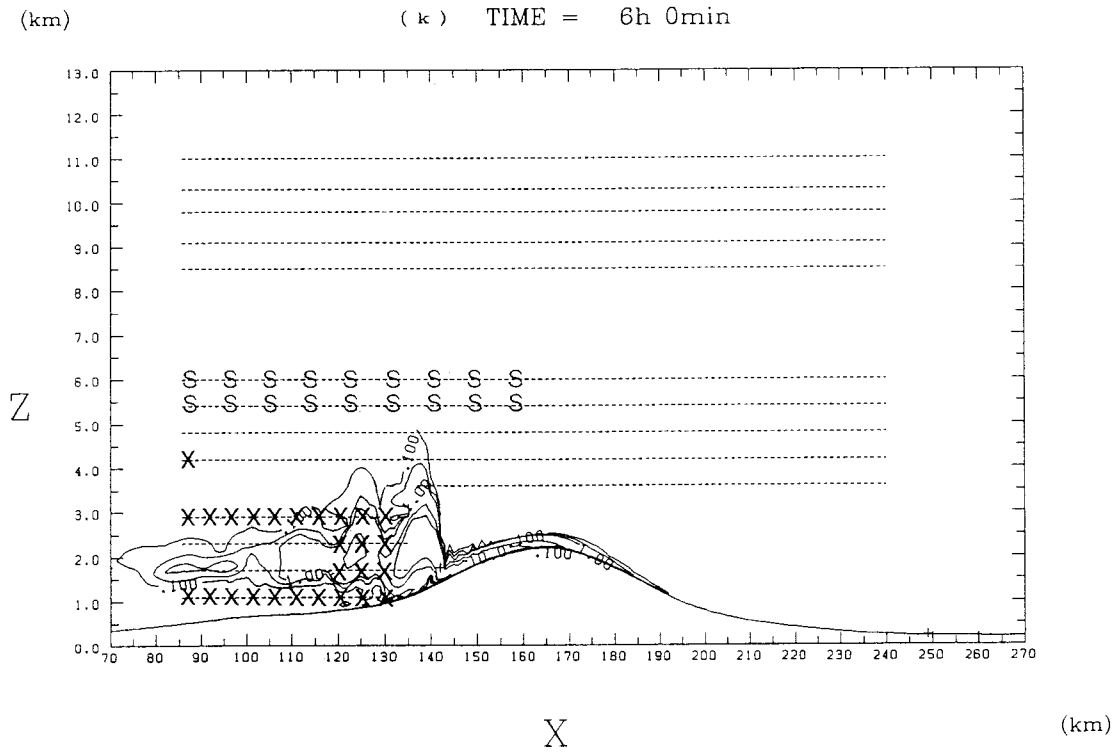

Fig. 15. Subgrid scale turbulent kinetic energy calculated by the E-ε model after 6 hours of integration in P9D3. The abscissa is the x-direction in km and the ordinate is the height in km. The contour interval is logarithmic (0.1, 0.5, 1, 5, 10) in m^2/sec^2. Airplane tracks are shown by dashed lines. Approximate locations of turbulence reported by on-board scientists are shown by crosses. Parts of dashed line with a character 'S' are approximate areas of sporadic turbulence reported by on-board scientists.

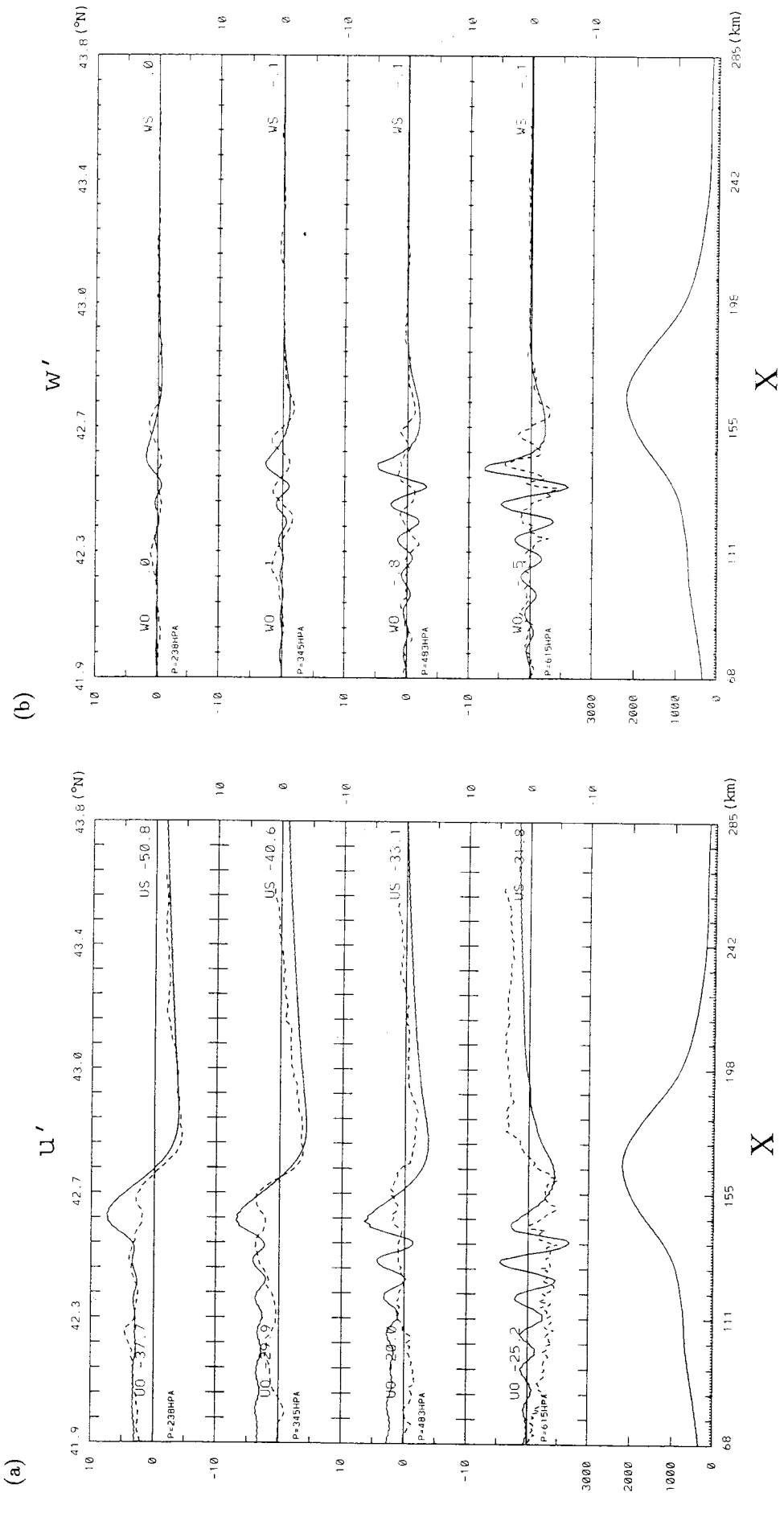

Fig. 16. Same as Fig. 10, except for P9D3 and the morning observation of 16 November 1990. The isobaric surfaces are 238 hPa, 345 hPa, 483 hPa and 615 hPa from the top to the bottom, respectively.

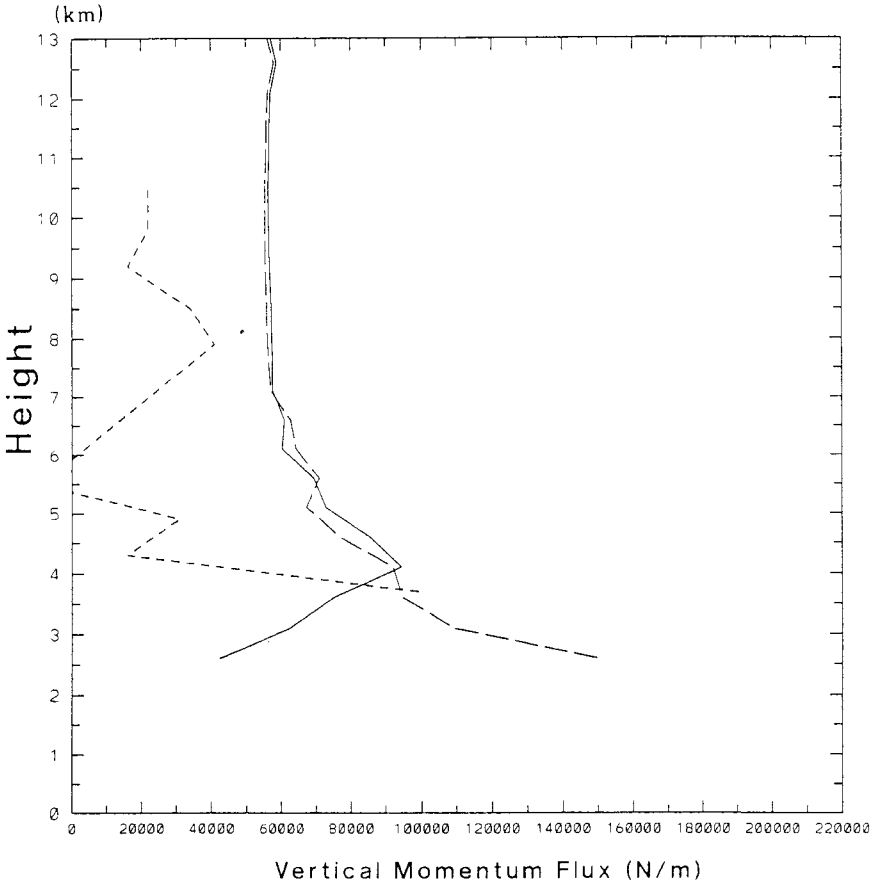

Fig. 17. Same as Fig. 11, except for P9D3.

5. Summary and Discussion

Two lee-wave events observed during PYREX were simulated using a two-dimensional, nonhydrostatic model initiated by upstream soundings. In spite of a very smooth bottom topography, the characteristics of lee waves were well simulated in both cases. We concluded that these lee waves were generated through nonlinear interactions of the principal wave, because the smooth mountain we used can directly excite mountain waves of the observed wavelength in negligible amplitude.

The upward momentum flux did not correspond with the airplane observation: the simulated flux was almost constant through the troposphere whereas the observation showed a rapid decrease above 4 km height in both cases. We also found that, in our two-dimensional model, mountain waves which have wavelengths longer than the lee waves control the vertical profile of the momentum flux: lee waves transport relatively very small amount of momentum flux in the vertical direction in almost all parts of the atmosphere. The exception was the layer below 4 km height in the case of P9D3. Because the strong turbulent dissipation was calculated to be around 2 km height in this case, this non-zero momentum flux of lee waves appears to be caused by the strong dissipation.

Figure 18 shows profiles of the square of Scorer parameter, l^2, based on the initial conditions of P3X1 and P9D3, defined by:

$$l^2 = \frac{N^2}{U^2} - \frac{1}{U}\frac{d^2U}{dz^2},$$

with buoyancy frequency N and the wind component perpendicular to the mountain U. In both cases, the Scorer parameter becomes very small in the middle troposphere. According to the linear theory (Smith, 1979, for example), these profiles of Scorer parameter are favorable to the occurrence of significant lee waves. In fact Tannhauser and Attié (1993) used the same vertical profiles of wind and temperature as in the case of P3X1 of this paper and succeeded in calculating the wavelength of the lee wave in good agreement with observation.

Looking to Fig. 18, we notice a slight difference in the Scorer parameter profile between P3X1 and P9D3: in the case of P9D3, it reduces rapidly around 4 km height and keeps small values above, whereas in P3X1 it diminishes gradually from 5.5 km to 7.5 km height and still has noticeable values occasionally above 8 km height. A steep (gentle) gradient of Scorer parameter indicates a strong (weak) trapping. This agrees with the fact that practically no

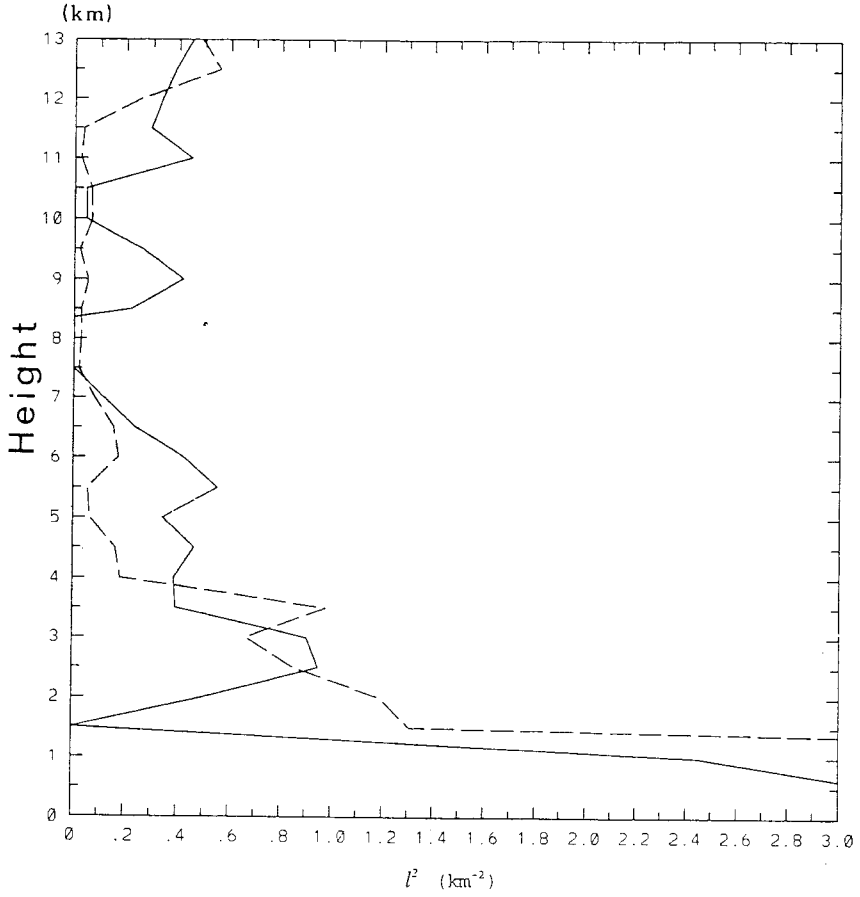

Fig. 18. Vertical profiles of l^2 in the case of IOP-3 (solid line) and the third day of IOP-9 (dashed line). These profiles are calculated by the initial conditions used in P3X1 and P9D3, respectively.

wave activity was found in the middle and the upper troposphere in the case of the third day of IOP-9, while a significant activity was present in the case of IOP-3.

Although the model simulates well the overall characteristics of mountain waves observed in IOP-3 and in the third day of IOP-9, the vertical momentum flux differs from observation. In order to simulate the vertical momentum flux well, it is necessary to simulate the principal wave well (which transports the major part of the upward momentum flux in the cases examined in this paper). The model clearly overestimates the principal wave in the upper troposphere.

The cause of this problem is believed to be the following: in the case of IOP-3 of PYREX, Beau (1992) and Bougeault *et al.* (1993) found that both the ageostrophic pressure force and the horizontal momentum advection through the lateral boundaries of a control box encompassing the mountain range were necessary to explain the horizontal momentum budget in their 3-dimensional, hydrostatic model. Furthermore, this effect was substantial in the upper troposphere. The importance of the horizontal momentum advection denotes that mountain waves observed during IOP-3 have a significant degree of three-dimensionality, even though the Pyrenees mountains seem to be approximately two-dimensional. The horizontal momentum budget in other cases is not available, but the three-dimensionality likely contaminates the vertical momentum flux profile also in the case of IOP-9.

In addition to the horizontal advection, Beau (1992) and Bougeault *et al.* (1993) pointed out that the situation was not stationary in the upper troposphere. As shown recently by Lott and Teitelbaum (1993a, 1993b), momentum fluxes of untrapped mountain waves under unsteady wind conditions are smaller than those under steady conditions.

These effects which cannot be incorporated in the two-dimensional stationary model used in this paper probably explain the difference of the observed vertical momentum flux with the simulated flux both in P3X1 and in P9D3. Thus, it is suggested that one must be careful in concluding that the horizontal mean wind will be decelerated albeit the upward momentum flux divergence is observed in one cross section of mountain as in the case of IOP-3. Still, nonhydrostatic 3-dimensional simulations and

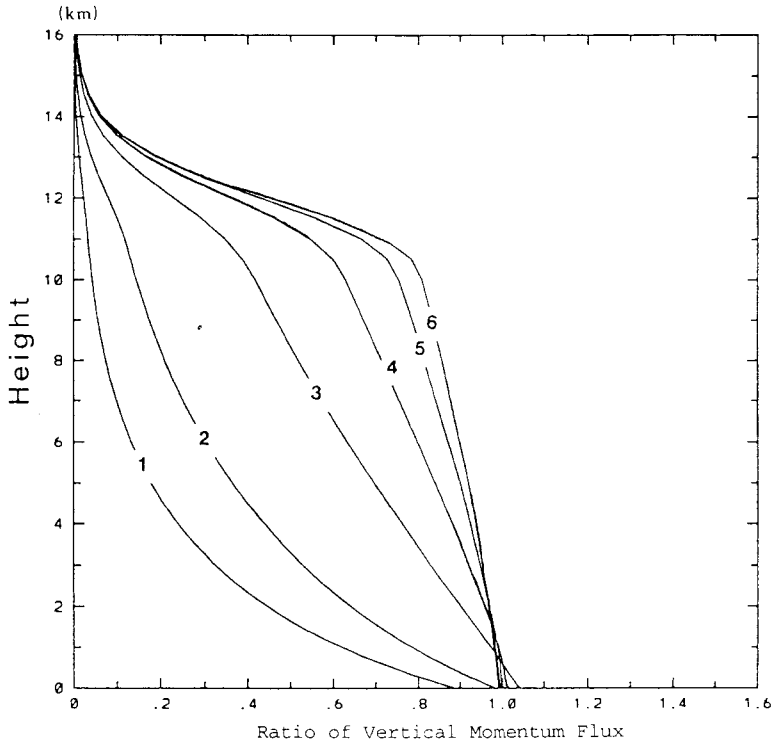

Fig. A1. Vertical profile of momentum flux ratio of model results to the linear theory. Numbers labeled on the lines are the integration time in hours.

the detailed analysis of the results are indispensable to clarify the effects of the non-steadiness and the horizontal momentum advection on the horizontal momentum budget. They are left to the future.

Acknowledgments

The PYREX experiment is a cooperative program supported by Météo-France, the Spanish Institute for meteorology, the CNRS/INSU (ARAT, PAMOS and PAMOY programs), the CNES, EDF, Région Midi-Pyrénées and the DLR.

We thank R. Smith of Yale Univ. and J. Stein of CNRM for helpful discussions and correspondence. We have greatly benefited from the aircraft momentum flux computations done by both K.R. Hoinka of DLR and J.L. Attié of Univ. Paul Sabatier.

Most of this work was performed during a visit of T.S. to CNRM, which was made possible by special grants from STA, Japan, and CNRS, France. The author gratefully acknowledges this support.

Appendix

Comparison of momentum flux in the model with the linear theory

In this appendix, a comparison of simulated momentum flux with the linear theory is presented to show the model's ability to reproduce the vertical momentum flux of the mountain wave. The linear theory predicts the vertical momentum flux at a constant mean wind speed U and the Brunt-Vaisala frequency N over a bell-shaped mountain as (see Smith, 1979, for example),

$$F_x = \int_{-\infty}^{\infty} \rho u' w' dx = -\frac{\pi}{4} \rho_0 N U h^2, \qquad \text{(A.1)}$$

where ρ_0 is the surface air density, π is the circular constant, h is the mountain height. This equation implicitly assumes that the mountain is wide and the atmosphere is hydrostatic.

The ratio of the model result to the linear theory (A.1) is shown in Fig. A1 in the case of $U = 15$ m/sec, $N = 0.01\,\mathrm{sec}^{-1}$, the mountain height $h = 10$ m and the half width of the mountain is 10 km. The model is run with the free-slip lower boundary condition, the model horizontal grid interval is 2.5 km and the vertical grid interval varies from 10 m to 500 m. The sponge layer is placed above 12 km height. This figure demonstrates that the model used in this paper agrees very well with the linear theory after 6 hours integration.

References

Aris, R., 1962; *Vectors, tensors, and the basic equations of fluid mechanics*, Prentice-Hall, Englewood Cliffs, 286 pp.

Attié, J.L., B. Benech, A. Druilhet and P. Durand, 1991; Comptes rendus scientifiques des expériences aéroportées réalisées avec l'ARAT et le Merlin VI

pendant PYREX, *TechnicalReportN°* 91–2, Laboratoire d'Aérologie, Université Paule Sabatier.

Beau, I., 1992; Evaluation des paramétrisation de l'effet orographique sous-maille dans les modèles de circulation générale à l'aide de PERIDOT 10 km, *Note de travail de l'ENM*, ENM, CNRM.

Bougeault, P., A. Jansa, B. Benech, B. Carrisimo, J. Pelon and E. Richard, 1990; Momentum budget over the Pyrénées: The PYREX experiment, *Bull. Amer. Meteor. Soc.*, **71**, 806–818.

Bougeault, P., A. Jansa, J.L. Attié, I. Beau, B. Benech, R. Benoit, P. Bessemoulin, J.L.'Caccia, J. Campins, B. Carrisimo, J.L. Champeaux, M. Crochet, A. Druilhet, P. Durand, A. Elkhalfi, P. Flamant, A. Genoves, M. Georgelin, K.P. Hoinka, V. Klaus, E. Koffi, V. Kotroni, C. Mazaudier, J. Pelon, M. Petitdidier, Y. Pointin, D. Puech, E. Richard, T. Satomura, J. Stein and D. Tannhauser, 1993; The atmospheric momentum budget over a major mountain range: First results of the PYREX field program, *Annales geophysicae*, **11**, 395–418.

Blockley, J.A. and T.J. Lyons, 1994; Airflow over a two-dimensional escarpment. III: Nonhydrostatic flow, *Q. J. R. Meteor. Soc.*, to be published.

Busch, N.E., S.W. Chang and R.A. Anthes, 1976; A multi-level model of the planetary boundary layer suitable for use with mesoscale dynamic models, *J. Appl. Meteor.*, **15**, 909–919.

Christie, D.R., 1989; Long nonlinear waves in the lower atmosphere, *J. Atmos. Sci.*, **46**, 1462–1491.

Clark, T.L. and M.J. Miller, 1991; Pressure drag and momentum fluxes due to the Alps. II: Representation in large-scale atmospheric models, *Q. J. R. Meteor. Soc.*, **117**, 527–552.

Detering, H.W. and D. Etling, 1985; Application of the E-ε turbulence model to the atmospheric boundary layer, *Boundary layer Meteor.*, **33**, 113–133.

Durran D.R., 1991; Orographic wave drag on the lower troposphere: The importance of trapped waves, *Proc. 8th Conf. Atmos. Ocean Waves and Stability*, 377–380.

Durran D.R. and J.B. Klemp, 1982; The effects of moisture on trapped mountain lee waves, *J. Atmos. Sci.*, **39**, 2490–2506.

Eliassen, A. and E. Palm, 1961; On the transfer of energy in stationary mountain waves, *Geofys. Publ.*, **22**, No. 3, 1–23.

Hoinka, K.P., 1984; Observations of a mountain-wave event over the Pyrenees, *Tellus*, **36A**, 369–383.

Hoinka, K.P. and T.L. Clark, 1991; Pressure drag and momentum fluxes due to the Alps. I: Comparison between numerical simulations and observations, *Q. J. R. Meteor. Soc.*, **117**, 495–525.

Iwasaki, T., S. Yamada and K. Tada, 1989; A parameterization scheme of orographic gravity wave drag with two different vertical partitionings. Part I: Impacts on medium-range forecasts, *J. Meteor. Soc. Japan*, **67**, 11–27.

Kim Y.J. and A. Arakawa, 1991; Assessment of gravity wave parameterization schemes using a mesoscale gravity-wave model, *Proc. 9th Conf. Num. Wea. Pred.*, 380–383.

Klemp, J.B. and D.K. Lilly, 1978; Numerical simulations of hydrostatic mountain waves, *J. Atmos. Sci.*, **35**, 78–107

Kuettner, J.P., 1986; The aim and conduct of ALPEX, *GARP Publ. Ser.*, **27**, 3–14.

Kurihara, Y., G.J. Tripoli and M.A. Bender, 1979; Design of a movable nested-mesh primitive equation model, *Mon. Wea. Rev.*, **107**, 239–249.

Lilly, D.K., 1978; A severe downslope windstorm and aircraft turbulence event induced by mountain wave, *J. Atmos. Sci.*, **35**, 59–77.

Lilly, D.K. and P.J. Kennedy, 1973; Observations of a stationary mountain wave and its associated momentum flux and energy dissipation, *J. Atmos. Sci.*, **30**, 1135–1152.

Lott, F. and H. Teitelbaum, 1993a; Topographic waves generated by a transient wind, *J. Atmos. Sci.*, **50**, 2607–2624.

Lott, F. and H. Teitelbaum, 1993b; Linear unsteady mountain waves, *Tellus*, **45A**, 201–220.

McFarlane, N.A., 1987; The effect of orographically excited gravity wave drag on the general circulation of the lower stratosphere and troposphere, *J. Atmos. Sci.*, **44**, 1775–1800.

Miller, M.J. and A.J. Thorpe, 1981; Radiation conditions for the lateral boundaries of limited-area numerical models, *Q. J. R. Meteor. Soc.*, **107**, 615–628.

Orlanski, I., 1976; A simple boundary condition for unbounded hyperbolic flows, *J. Comput. Phys.*, **21**, 251–269.

Palmer, T.N., G.J. Shutts and R. Swinbank, 1986; Alleviation of a systematic westerly bias in general circulation and numerical weather prediction models through an orographic gravity wave drag parametrization, *Q. J. R. Meteor. Soc.*, **112**, 1001–1039.

Phillips, N.A. and J. Shukla, 1973; On the strategy of combining coarse and fine grid meshes in numerical weather prediction, *J. Appl. Meteor.*, **12**, 763–770.

Richard, E., P. Mascart and E.C. Nickerson, 1989; The role of surface friction in downslope windstorm, *J. Appl. Meteor.*, **28**, 241–251.

Rodi, W., 1985; Calculation of stably stratified shear-layer flows with a buoyancy-Extended K-ε turbulence model, *Turbulence and diffusion in stable environments*, Ed. by J.C.R. Hunt, Oxford, 111–140.

Sasaki, H. and T. Satomura, 1991; Numerical experiments on convergence cloud bands over the northern part of the Japan Sea, *J. Meteor. Soc. Japan*, **69**, 375–388.

Satomura, T., 1989; Compressible flow simulations on numerically generated grids, *J. Meteor. Soc. Japan*, **67**, 473–482.

Scorer, R.S., 1949; Theory of waves in the lee of mountains, *Q. J. R. Meteor. Soc.*, **75**, 41–56.

Sharman, R.D. and M.G. Wurtele, 1983; Ship waves and lee waves, *J. Atmos. Sci.*, **40**, 396–427.

Shieh, C.F., 1984; Three-dimensional grid generation using elliptic equations with direct grid distribution control, *AIAA Journal*, **22**, 361–364.

Shutts, G.J., 1992; Observation and numerical model simulation of a partially trapped lee wave over the Welsh mountains, *Mon. Wea. Rev.*, **120**, 2056–2066.

Shutts, G.J. and A. Broad, 1993; A case study of lee waves over the Lake District in northern England, *Q. J. R. Meteor. Soc.*, **119**, 377–408.
Smith, R.B., 1979; The influence of mountain on the atmosphere, *Adv. Geophy.*, **21**, 87–230.
Tannhauser, D. and J.L. Attié, 1993: Optical and quantum mechanical analogs for trapped and leaky lee waves, submitted to *Tellus*.
Wallace, J.M., S. Tibaldi and A.J. Simmons, 1983; Reducing of systematic forecast errors in the ECMWF model through the introduction of an envelope orography, *Q. J. R. Meteor. Soc.*, **109**, 683–717.
Vergeiner, I., 1971; An operational linear lee wave model for arbitrary basic flow and two-dimensional topography, *Q. J. R. Meteor. Soc.*, **97**, 30–60.

ピレネー山脈における風下波の数値シミュレーション

里村雄彦
(気象研究所)
Philippe Bougeault
(フランス国立気象研究センター)

二次元非静水圧の圧縮モデルを用い、PYREXプログラム期間中に観測された2つの風下波の事例について数値シミュレーションを行った。それぞれの事例について、モデルの初期地を上流のある1点での高層観測値から作成した。モデル地形は、実際の地形から波長10 km以下の凸凹を平滑化したものを使っている。

計算の結果、モデルは風下波の波長、振幅、出現位置をうまく再現することがわかった。モデル地形が風下波の波長成分(約10 km)をほとんど含んでいないことから、計算結果と観測の一致は、観測された風下波が長い波長の山岳波の非線形相互作用によって励起されたことを強く示唆している。また、感度試験を行った結果、風下波の位相は平均風のわずかな変化に敏感なこと、短波長の地形の存在によって風下波の振幅が大きくなることも示された。

運動量の鉛直フラックスについても観測との比較を行った結果、観測の下限である高度4 km付近においては、モデルと観測ともIOP-3でほぼ-15×10^4 N/m、IOP-9第3日でほぼ$+10 \times 10^4$ N/mと、両者の対応は良かった。しかし、高度4 km以上で運動量フラックスの絶対値の急速な減少が観測されたのに対し、モデルではほぼ一定となっていることが分かった。このような、モデルの中上部対流圏での運動量フラックスの過大評価は、運動量フラックスの大半を担っている長い波長の山岳波の振幅をモデルが過大に表現したためである。その原因として、現実大気における平均風の時間変化や横方向の運動量フラックス発散が考えられることを示した。